Journal of Wind Engineering & Industrial Aerodynamics 196 (2020) 104028

Contents lists available at ScienceDirect

Journal of Wind Engineering & Industrial Aerodynamics

journal homepage: www.elsevier.com/locate/jweia

Effects of Reynolds number in the range from 1.6×10^3 to 1.6×10^6 on the flow fields in tornado-like vortices by LES: A systematical study

Zhenqing Liu [a,*], Shuyang Cao [b], Heping Liu [c], Xugang Hua [d], Takeshi Ishihara [e]

[a] School of Civil Engineering and Mechanics, Huazhong University of Science and Technology, Wuhan, Hubei, China
[b] State Key Laboratory for Disaster Reduction in Civil Engineering, Tongji University, Shanghai, China
[c] Department of Civil and Environmental Engineering, Washington State University, Pullman, WA, USA
[d] Key Laboratory for Wind and Bridge Engineering of Hunan Province, College of Civil Engineering, Hunan University, Changsha, Hunan, China
[e] Department of Civil Engineering, School of Engineering, The University of Tokyo, Tokyo, Japan

ARTICLE INFO

Keywords:
Large-eddy simulations
Reynolds number
Tornado-like vortices
Mean and turbulent flow
Momentum budget
Similarity

ABSTRACT

In the present study, the Reynolds effects on the flow fields of tornadoes in the range from 1.6×10^3 to 1.6×10^6 are systematically investigated. Large eddy simulations are adopted. Representative parameters including instantaneous Q value, mean velocities, root mean square of velocity fluctuations, skewness and kurtosis of the velocities, as well as the momentum budget is systematically investigated. It is noteworthy that if Re is sufficiently high, the major balance in the momentum budget between the radial pressure gradient and the centrifugal force even will be reached even at the elevation close to the ground. Furthermore, the ratio between the height and the radius of the location where the tangential velocity is peaked exhibit an almost linear relationship with $Re^{-1/3}$, of which the slope decreases with the rise in the swirl ratio.

1. Introduction

Extensive knowledge of the flow fields in the tornado-like vortices as a function of swirl ratio, S, have been obtained experimentally [Ward (1972); Wan and Chang (1972); Church et al. (1979); Baker (1981); Mitsuta and Monji (1984); Monji (1985); Haan et al. (2008); Matsui and Tamura (2009); Tari et al. (2010), etc.] and numerically [Rotunno (1977); Wilson and Rotunno (1986); Nolan and Farrell (1999); Lewellen et al. (1997); Lewellen et al. (2000); Hangan and Kim (2008); Ishihara et al. (2011); Ishihara and Liu (2014), etc.]. Swirl ratio is defined as $S=\Gamma r_0/2Qh$, where Γ is the background circulation, r_0 is the characteristic radius usually corresponding to the radius of the updraft region, h is the height that usually corresponds to the depth of the inflow layer and Q is the volume flow rate per unit axial length. Therefore, the swirl ratio can be seen as the ratio of rotation moment to the radial moment. When using the guide-vanes at the bottom of the tornado simulator to provide the swirling of the flow, the swirl ratio can be simplified as $S=\tan(\theta)\ r_0/2h$, where θ is the angle of the guide vanes. As increasing the swirl ratio, the centrifugal force will increase and, as a result, the expansion of the tornado will occur [Davies-Jones (1973)]. Various developments of the tornado-like vortices as a function of swirl ratio have been examined [Hangan and Kim (2008); Tari et al. (2010); Liu and Ishihara (2015a, 2015b); Kashefizadeh et al. (2019); Yuan et al. (2019), etc.]. As the value of the swirl ratio is increased, the vortex goes through various stages, as depicted in Fig. 1. When the swirl ratio is small, there is no concentrated vortex at the surface, see Fig. 1a. For larger values, a concentrated vortex does appear at the surface, and at some height above it, there is a vortex breakdown where the flow changes from a single-celled vortex to a multi-celled vortex. As S is further increased, the altitude of the vortex breakdown decreases [Church et al. (1979), Church et al. (1979)]. This state has been referred to as a "drowned vortex jump" (DVJ). When S is further increased, the vortex breakdown reaches the surface and the vortex changes to a "two-celled'' structure, Fig. 1c, where there is a downward recirculation in the vortex core and the radius of maximum winds substantially increases [Ward (1972); Matsui and Tamura (2009); Tari et al. (2010), etc.]. Still larger values of S result in the appearance of multiple vortices rotating around the vortex core as shown in Fig. 1d [Mitsuta and Monji (1984); Monji (1985), etc.].

With the advancement of the measuring techniques and the enhancement of the computers performance, numerous findings have been achieved. The researches about the tornado in the area of wind engineering primarily cover four aspects, including the flow fields in the near ground boundary layer [Wan and Chang (1972), Rotunno (1977), Church et al. (1979), Mitsuta and Monji (1984), Wilson and Rotunno (1986), Nolan and Farrell (1999), Lewellen et al. (1997, 2000), Lewellen

* Corresponding author.
E-mail address: liuzhenqing@hust.edu.cn (Z. Liu).

https://doi.org/10.1016/j.jweia.2019.104028
Received 16 April 2019; Received in revised form 24 July 2019; Accepted 2 November 2019
Available online 15 November 2019

Nomenclature

Lowercase

a	aspect ratio
d	distance to the closest wall
d_c	depth of the convergence flow
h	height of the inlet layer
h_{vmax}	height of the location maximum tangential velocity occurs
$\tilde{p}$	filtered pressure
r_0	radius of the updraft hole
r_t	radius of the exhaust outlet
r_{vmax}	radius of the location maximum tangential velocity occurs
(u,v,w)	r.m.s of the radial, tangential and vertical fluctuations
$\tilde{u}_i$	filtered velocity
u_*	friction velocity
$u_{\max}$	maximum radial velocity fluctuation
(x, y, z)	Cartesian coordinates

Capitals

A_{ru}	radial advection term in radial momentum budget
A_{zu}	vertical advection term in radial momentum budget
C_r	centrifugal force term in radial momentum budget
C_s	Smagorinsky constant
D_u	diffusion term in radial momentum budget
Ku_{u_i}	kurtosis of the fluctuating velocities
L_s	SGS mixing length
P_r	radial pressure gradient term in radial momentum budget
Q	flow rate
Re	Reynolds number
S	swirl ratio
Sk_{u_i}	skewness of the fluctuating velocities
$\tilde{S}_{ij}$	rate-of-strain tensor
T_u	turbulent force term in radial momentum budget
(U,V,W)	mean radial, tangential and vertical velocities
W_0	velocity at the outlet

Greek symbols

Δt	time step size
Δt^*	convective time units
Δx_i	grid size
δ_{ij}	Kronecker delta
δ_n	distance between cell and wall
θ	inflow angle
κ	Kármán constant
Λ	volume of a computational cell
μ	viscosity
μ_t	SGS turbulent viscosity
ρ	density of the flow
τ_{ij}	SGS stress

Abbreviations

CFL	Courant Friedrichs Lewy
LES	large eddy simulations
PDF	probability density function
SGS	subgrid-scale
TKE	turbulence kinetic energy

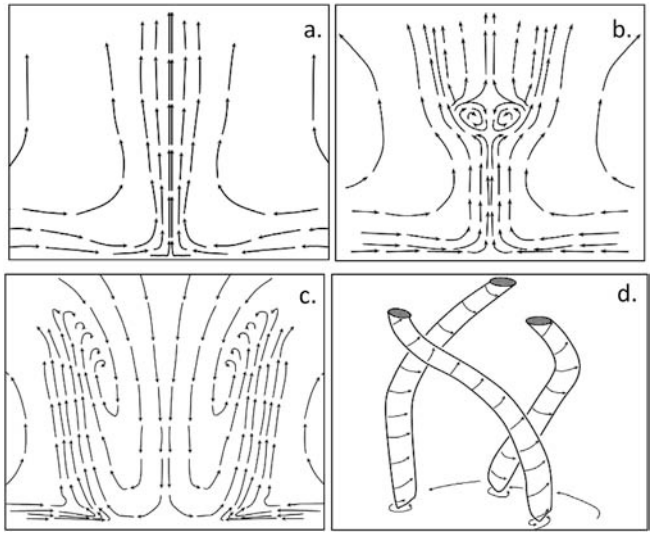

Fig. 1. Illustrations of four stages as the swirl ratio is increased from zero: (a) single celled vortex; (b) surface vortex with vortex breakdown above the surface; (c) two celled vortex; and (d) multi vortex with stagnant core.

and Lewellen (2007), Haan, et al. (2008), Kuai et al. (2008), Tari, et al. (2010), Zhang and Sarkar (2012), Lombardo, et al. (2015), Liu and Ishihara (2015a), Kim and Matsui (2017), Refan and Hangan (2018), Eguchi, et al. (2018), Liu, et al. (2018), Gairola and Bitsuamlak (2019), Ashton, et al. (2019)], the effects exerted by the tornado translation and the ground roughness [Natarajan and Hangan (2012); Sabareesh et al. (2013); Liu and Ishihara (2016); Wang et al. (2017)], the tornado-induced wind loads on structures [Hu et al. (2011); Yang et al. (2011); Rajasekharan et al. (2012); Rajasekharan et al. (2013); Case et al. (2014); Strasser et al. (2016); Wang et al. (2016); Liu and Ishihara (2015b); Feng and Chen (2018); Cao et al. (2018); Razavi and Sarkar (2018); Cao et al. (2019)], as well as the tornado-induced debris [Maruyama (2011); Zhou et al. (2014); Baker and Sterling (2018)]. Most of the researches are conducted using the experimental tornado simulators, in which three types of tornado simulator have been developed. Ward type simulator was developed by Ward (1972), providing the swirling of the flow by the rotating screen or the guide vanes mounted on the ground. Iowa State University (ISU) type simulator was designed by Haan et al. (2008), swirling the flow with the use of the guide vanes mounted on the top of simulator. Furthermore, WindEEE type simulator developed by Refan et al. (2014) swirls the flow through the fans surrounding the inlet.

The effects of Reynolds number have been investigated by Monji (1985), in which the distinct dependency of the types of the tornado in the low Re region ($\mathrm{Re} = L^*{\cdot}U^*/\upsilon < 3.0 \times 10^4$) is found through a Ward type simulator, where, L^* and U^* are the characteristic velocity and length, respectively, $\upsilon = \mu/\rho$ is the kinematic viscosity, μ is the viscosity, ρ is the density of the fluid. Refan and Hangan (2016, 2018) analyzed the tornadoes using WindEEE tornado simulator with radial Reynolds number $\mathrm{Re_r} = Q/(2\pi\upsilon)$ ranging from 1.6×10^4 to 2.0×10^6, where, Q is the flow rate per unit axial length. Besides, $\mathrm{Re_r} = 4.5 \times 10^4$ is considered as the critical value beyond which the surface static pressure is quasi-independent of $\mathrm{Re_r}$. Tang et al. (2018) experimentally studied the Reynolds effects on the tornado-like vortices in a range from $\mathrm{Re_r} = 2.39 \times 10^5$ to $\mathrm{Re_r} = 3.91 \times 10^5$. However, the mentioned examinations primarily considered the macro parameters, such as maximum tangential velocities, maximum radial velocity, or surface pressure.

In this study, large eddy simulations (LES) were conducted and the tornadoes with $S = 1.0$ and $S = 4.0$ were modeled. On the one hand, $S = 1.0$ is the transitional stage sensitive to the variation of the flow conditions. On the other hand, $S = 4.0$ has been observed as the case of one full scale tornado according to the study by Liu and Ishihara (2015a). For the Reynolds number, four values ranging from $\mathrm{Re} = 1.6 \times 10^3$ to

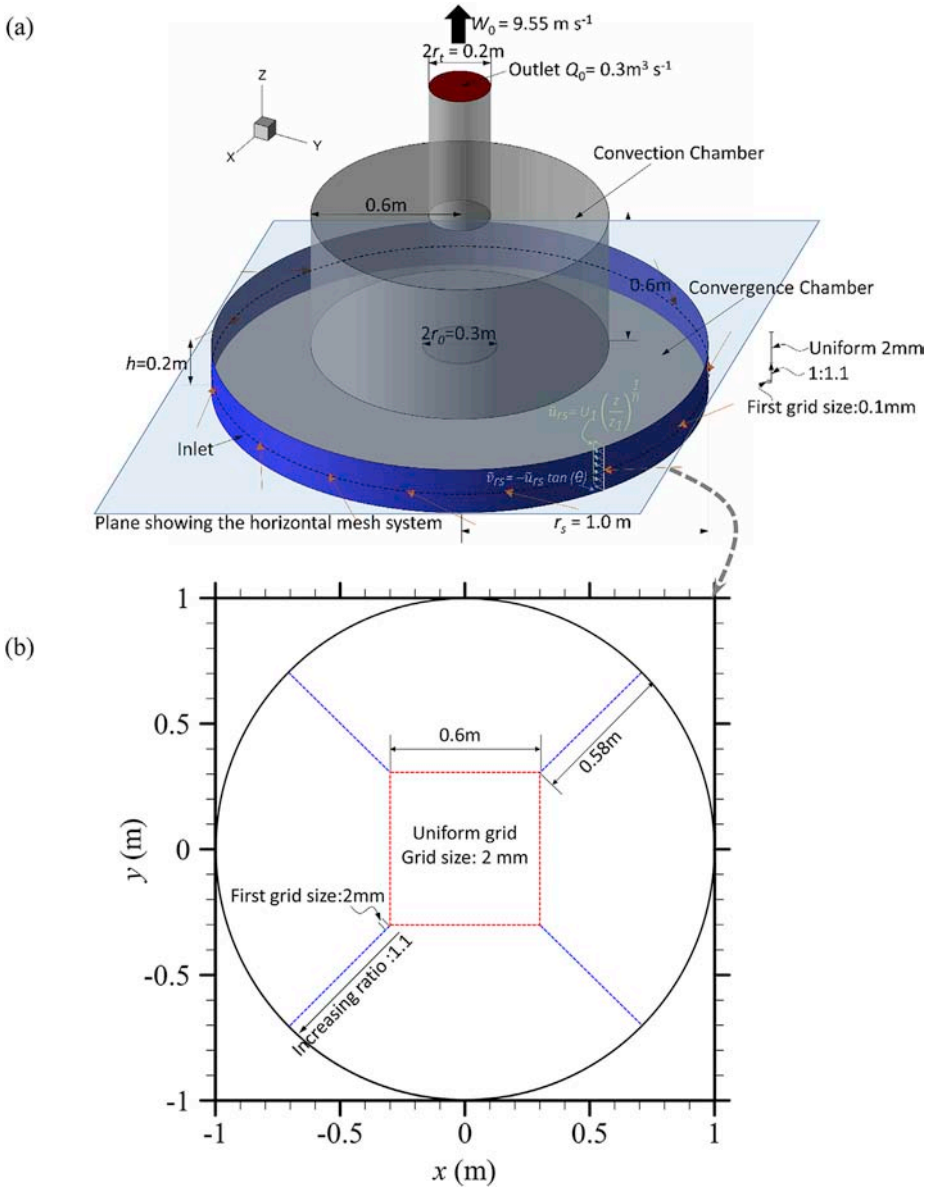

Fig. 2. Configurations of (a) the computational domain and (b) the horizontal mesh system.

Table 1
Parameters of the tornado simulator.

Height of the inlet layer: h	200 mm
Radius of the updraft hole: r_0	150 mm
Radius of the exhaust outlet: r_t	100 mm
Radius of the convergence region: r_s	1000 mm
Velocity at the outlet: W_0	9.55 m s^{-1}
Total outflow rate: Q_0	0.3 m^3/s

$\mathrm{Re} = 1.6 \times 10^6$ were selected.

The rest of this paper is organized as follows. Section 2 provides detailed introduction of the numerical model. The results of the simulations are presented in section 3. The instantaneous flow fields visualized by Q-criterion are presented to develop a general idea of the effects from S and Re, followed by the presentation of the mean and fluctuation of the velocities. The skewness and kurtosis reflecting the properties of probability density function (PDF) of the velocities are examined. Subsequently, to clarify the major contributions of the averaged flow fields

Table 2
Summary of the boundary conditions.

Locations	Boundary type	Expression
Outlet of the simulator	Outlet	$\partial\tilde{u}_i/\partial n = 0$, $\partial\tilde{p}/\partial n = 0$, $\tilde{w} = 9.55\,\mathrm{ms}^{-1}$
Surrounding walls of the simulator	Non-slip wall	$\partial\tilde{p}/\partial n = 0$, $\tilde{u}_i = 0$
Inlet of the chamber	Velocity inlet	$\tilde{u}_i$ determined by Eq. (8), $\partial\tilde{p}/\partial n = 0$

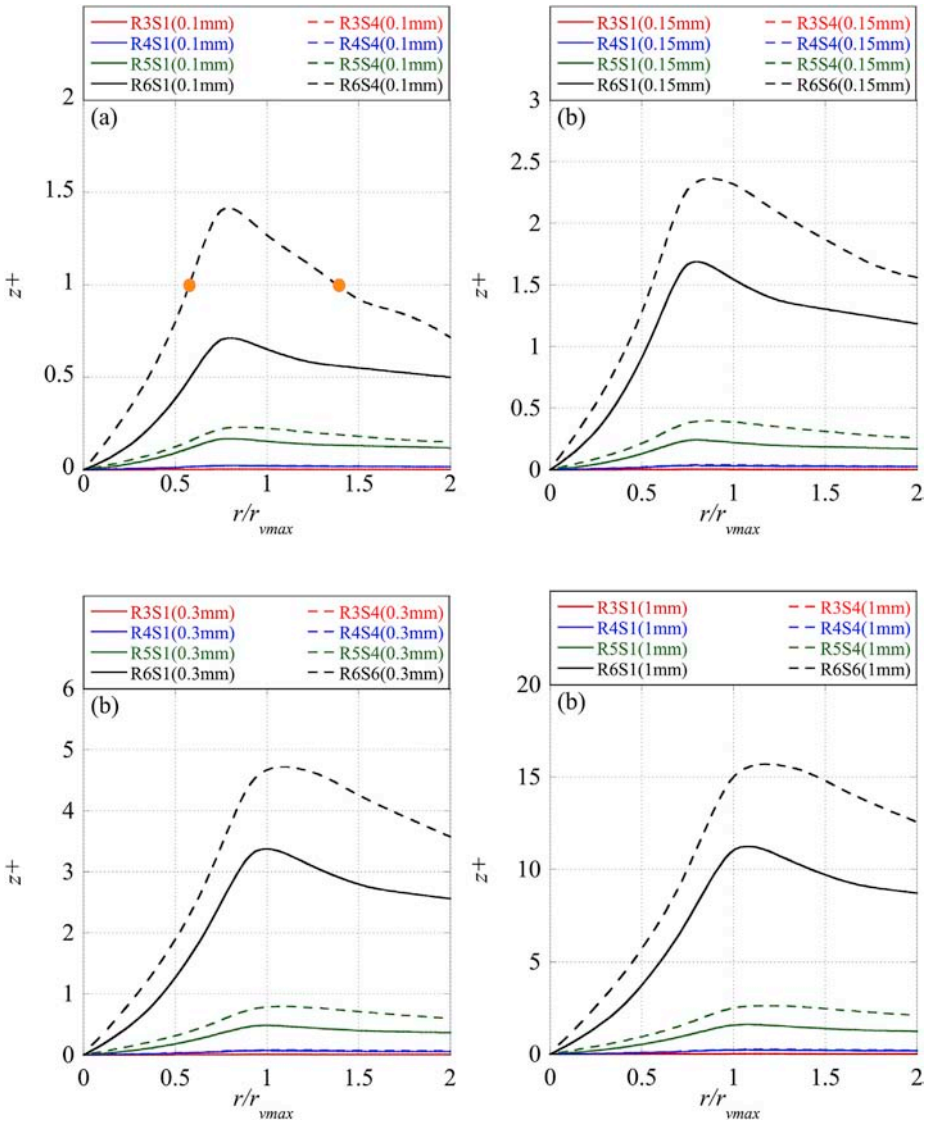

Fig. 3. z^+ as a function of radial distance for refined grids, heights of the wall-attached grid equals to (a) 0.1 mm, (b) 0.15 mm, (c) 0.3 mm, and (d) 1.0 mm.

Table 3
Summary of numerical schemes.

Time discretization scheme	Second-order implicit scheme	Cs number	0.032
Space discretization scheme	FVM second-order central difference scheme	SGS model	Smagorinsky-Lilly
Non-dimensional time step size: $\Delta t W_0/2r_0$	0.003	CFL number: $\Delta t \Sigma \bar{u}_i/\Delta x_i$	<2
Turbulence model	Large eddy simulation	Velocity-pressure decoupling method	SIMPLE

Table 4
Case settings.

Case name	Swirl ratio S	Reynolds number Re	Radial Reynolds number Re_r	z + range	r_{vmax} (mm)	h_{vmax} (mm)
R3S1	1.0	1.6×10^3	1.3×10^2	[0,0.006]	25	/
R4S1	1.0	1.6×10^4	1.3×10^3	[0,0.045]	14	15.8
R5S1	1.0	1.6×10^5	1.3×10^4	[0,0.212]	21	8.8
R6S1	1.0	1.6×10^6	1.3×10^5	[0,0.721]	29	7.1
R3S4	4.0	1.6×10^3	1.3×10^2	[0,0.009]	44	22.0
R4S4	4.0	1.6×10^4	1.3×10^3	[0,0.053]	46	11.0
R5S4	4.0	1.6×10^5	1.3×10^4	[0,0.347]	36	4.5
R6S4	4.0	1.6×10^6	1.3×10^5	[0,1.482]	64	4.3

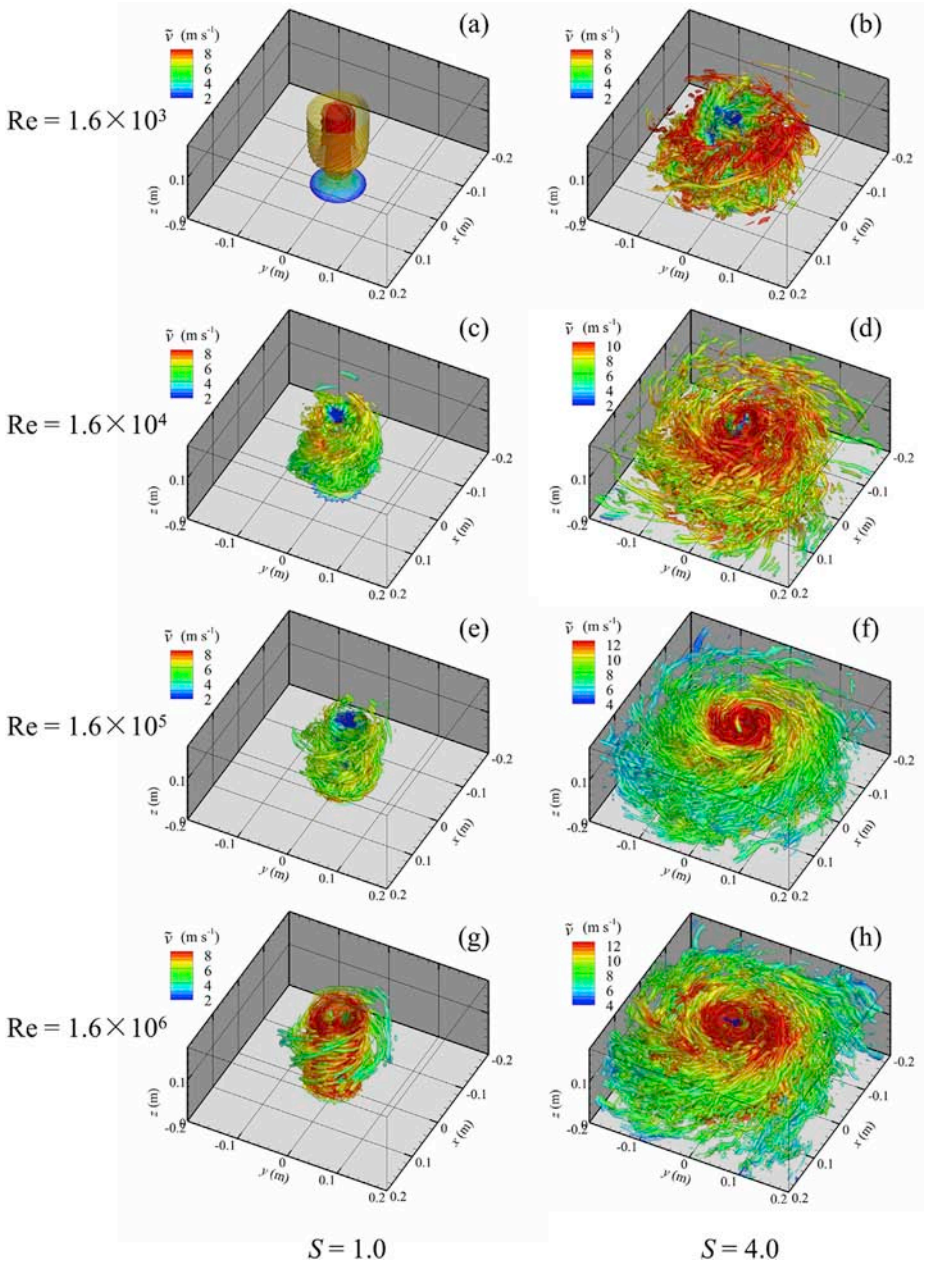

Fig. 4. Iso-surfaces of Q values for (a) R3S1, (b) R3S4, (c) R4S1, (d) R4S4, (e) R5S1, (f) R5S4, (g) R6S1, and (h) R6S4. The values of Q for plotting the iso-surfaces in the cases of $S = 1.0$ are ± 20000, and in the cases of $S = 4.0$ are ± 50000. The iso-surfaces are further colored by the instantaneous tangential velocities.

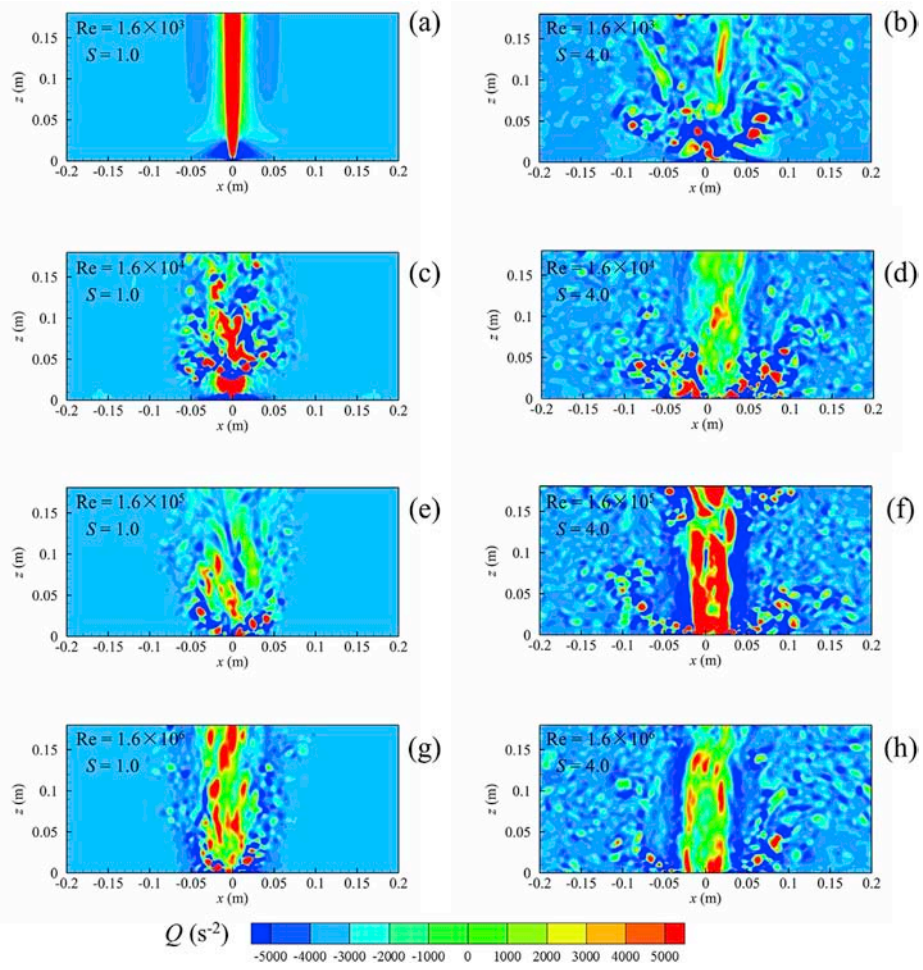

Fig. 5. Instantaneous contour of Q values on the vertical slice crossing the center of the tornado simulator for (a) R3S1, (b) R3S4, (c) R4S1, (d) R4S4, (e) R5S1, (f) R5S4, (g) R6S1, and (h) R6S4.

and the turbulence, the momentum budget are investigated. Finally, the effects of the S and Re on the similarity parameter are summarized.

2. Numerical model

2.1. Governing equations

In the LES strategy, large eddies are explicitly resolved, while the small eddies are parameterized by SGS models. The governing equations are usually obtained by filtering the time-dependent Navier–Stokes equations in Cartesian coordinates (x, y, z):

$$\frac{\partial \rho \tilde{u}_i}{\partial x_i} = 0 \tag{1}$$

$$\frac{\partial \rho \tilde{u}_i}{\partial t} + \frac{\partial \rho \tilde{u}_i \tilde{u}_j}{\partial x_j} = \frac{\partial}{\partial x_j}\left(\mu \frac{\partial \tilde{u}_i}{\partial x_j}\right) - \frac{\partial \tilde{p}}{\partial x_i} - \frac{\partial \tau_{ij}}{\partial x_j} + f_i \tag{2}$$

where $\tilde{u}_i$ and $\tilde{p}$ are the filtered velocity and pressure, respectively; μ is the viscosity; ρ is the density; and τ_{ij} is the SGS stress. To close the equations for the filtered velocities, a model for the anisotropic residual stress tensor τ_{ij} is needed, which is obtained as:

$$\tau_{ij} = -2\mu_t \tilde{S}_{ij} + \frac{1}{3}\tau_{kk}\delta_{ij} \tag{3}$$

$$\tilde{S}_{ij} = \frac{1}{2}\left(\frac{\partial \tilde{u}_i}{\partial x_j} + \frac{\partial \tilde{u}_j}{\partial x_i}\right) \tag{4}$$

where μ_t denotes the SGS turbulent viscosity; $\tilde{S}_{ij}$ refers to the rate-of-strain tensor for the resolved scale, and δ_{ij} is the Kronecker delta. The Smagorinsky-Lilly model is used to parameterize the SGS turbulent viscosity [Ferziger and Peric (2002)] as:

$$\mu_t = \rho L_s^2 |\tilde{S}| = \rho L_s^2 \sqrt{2\tilde{S}_{ij}\tilde{S}_{ij}} \tag{5}$$

$$L_s = min\left(\kappa d,\ C_s \Lambda^{1/3}\right) \tag{6}$$

where L_s stands for the SGS mixing length; κ represents the von Kármán constant (= 0.42); d is the distance to the closest wall, and Λ is the volume of a computational cell. Here, C_s denoting the Smagorinsky constant is set to a value of 0.032 following the study by Liu and Ishihara (2015a).

When the cells are in the viscous sublayer, the shear stresses are obtained from the viscous stress-strain relation:

$$\frac{\tilde{u}}{u_*} = \frac{\rho u_* \delta_n}{\mu} \tag{7}$$

where u_* is the friction velocity, μ is the viscosity and δ_n is the distance between the cell center and the wall.

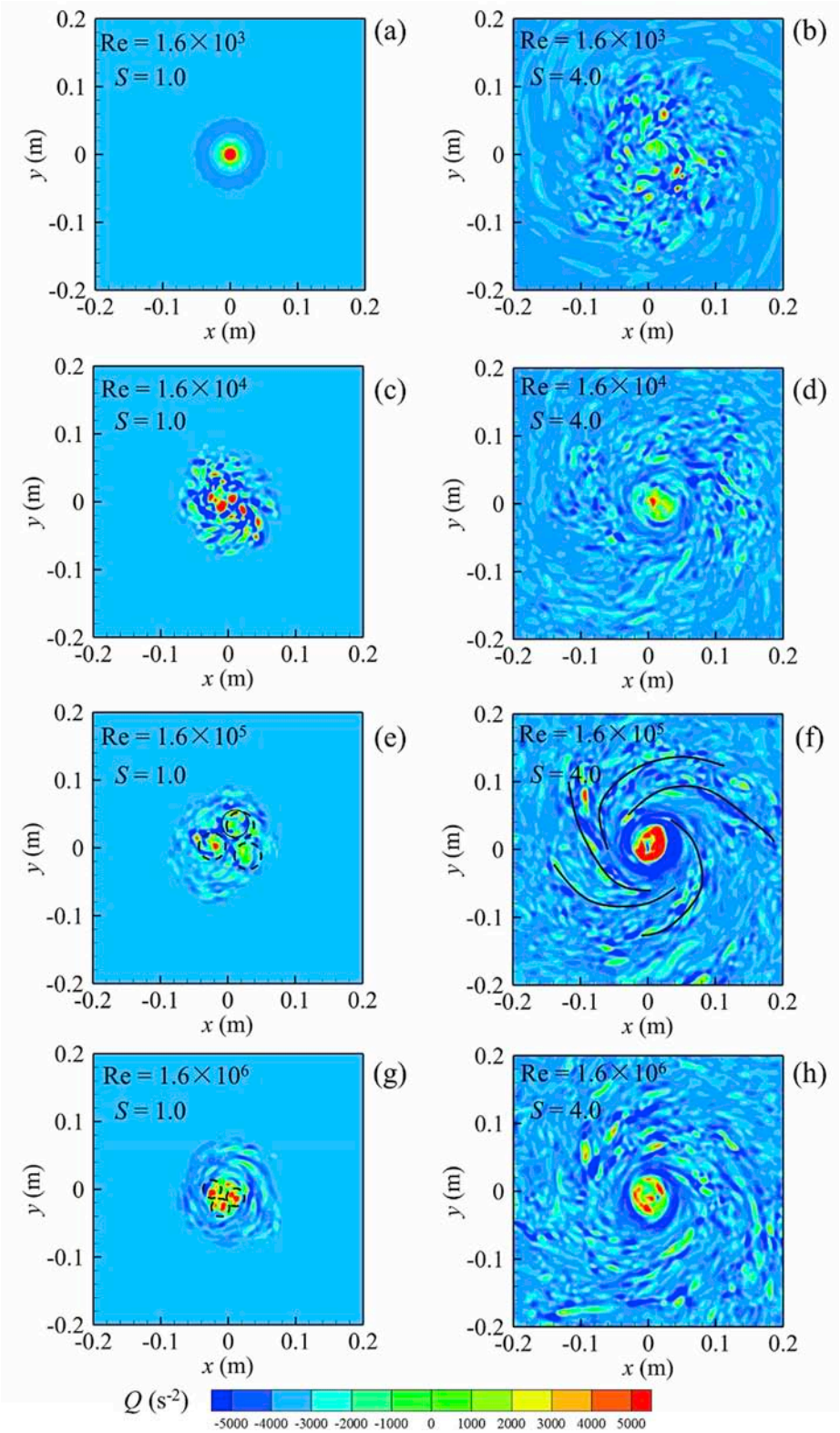

Fig. 6. Instantaneous contour of *Q* values on the horizontal slice with a height of 0.1 m for (a) R3S1, (b) R3S4, (c) R4S1, (d) R4S4, (e) R5S1, (f) R5S4, (g) R6S1, and (h) R6S4. The dashed circles indicate the sub-vortex and the solid lines shows the "swaths" around the tornado core.

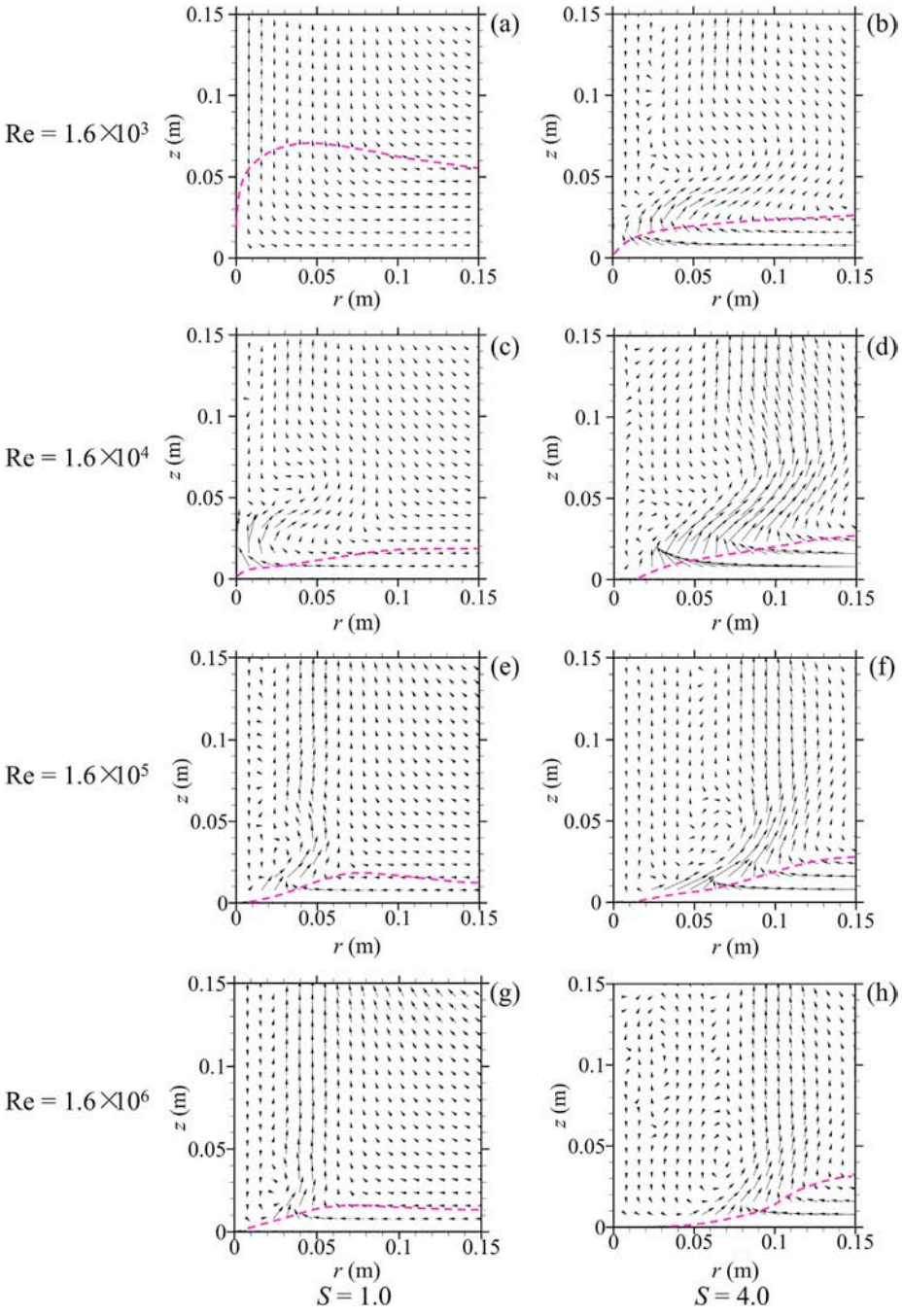

Fig. 7. Distributions of the vectors on the vertical slice crossing the center of the tornado (a) R3S1, (b) R3S4, (c) R4S1, (d) R4S4, (e) R5S1, (f) R5S4, (g) R6S1, and (h) R6S4. The pink dashed lines show the depth of the convergence flow determined by the locations with 0.1 U_{max}. (For interpretation of the references to color in this figure legend, the reader is referred to the Web version of this article.)

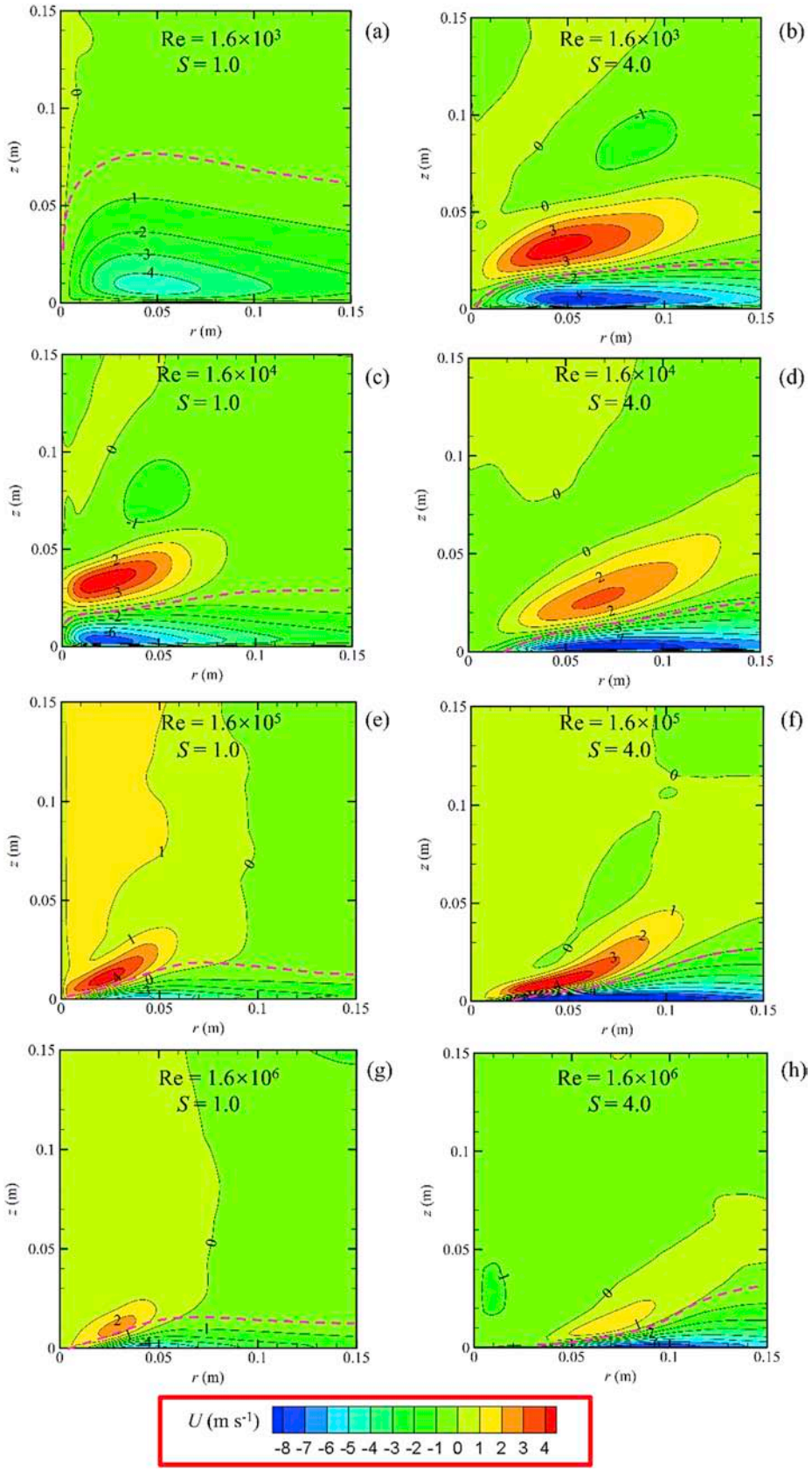

Fig. 8. Distributions of the time-space averaged radial velocity on the vertical slice crossing the center of the tornado (a) R3S1, (b) R3S4, (c) R4S1, (d) R4S4, (e) R5S1, (f) R5S4, (g) R6S1, and (h) R6S4. The pink dashed lines show the depth of the convergence flow determined by the locations with 0.1 U_{max}. (For interpretation of the references to color in this figure legend, the reader is referred to the Web version of this article.)

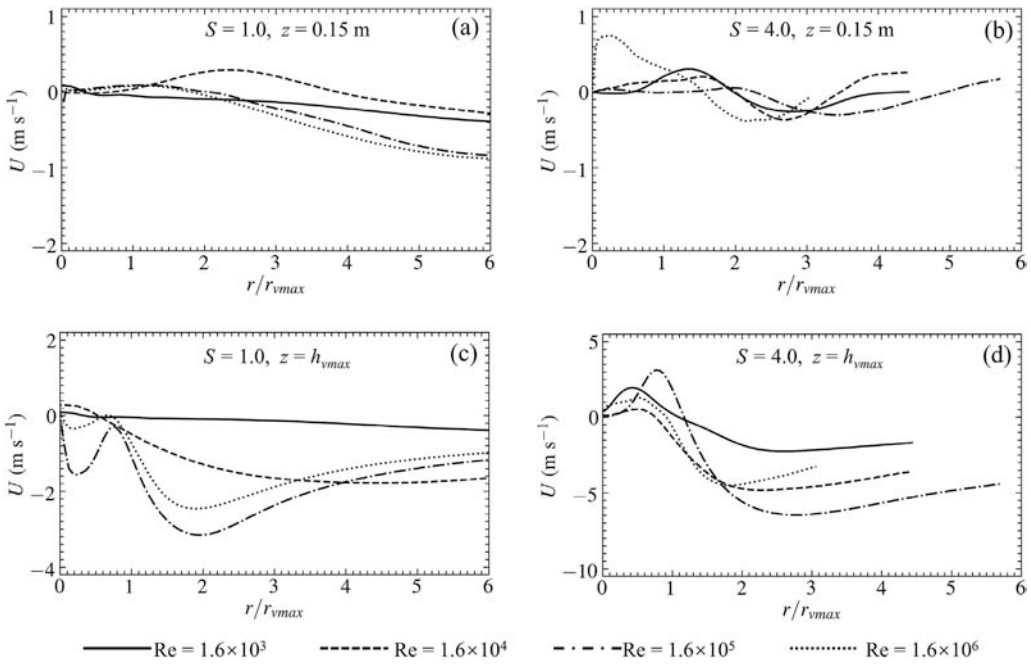

Fig. 9. Radial distribution of the time-space averaged radial velocity for (a) $S = 1.0$ at $z = 0.15$ m, (b) $S = 4.0$ at $z = 0.15$ m, (c) $S = 1.0$ at $z = h_{vmax}$, and (d) $S = 4.0$ at $z = h_{vmax}$.

2.2. Computational domain and mesh

A Ward-type simulator is employed, of which the configurations are illustrated in Fig. 2a, according to the experiment by Matsui and Tamura (2009). The height of the inlet layer, h, and the radius of the updraft hole, r_0, are set as 200 mm and 150 mm, respectively. The flow rate $Q_0 = \pi r_t^2 W_0 = 0.3\ \mathrm{m}^3\ \mathrm{s}^{-1}$, where $r_t = 250$ mm denotes the radius of the exhaust outlet and $W_0 = 9.55\ \mathrm{ms}^{-1}$ represents the velocity at the outlet. The geometrical parameters are listed in Table .1.

For the grid system of the tornado simulator, fine mesh is adopted in the convergence region, that is split into five regions as illustrated in Fig. 2b. Close to the center of the convergence region, an area with a square shape is considered to exhibit a horizontal resolution of 2 mm. This square shape has the size of 0.6 m, two times that of the diameter of the outlet of the updraft hole. The horizontal grid size from the boundary of this square-shape area to the outlet of the convergence region is enlarged at a ratio of 1.1. In the vertical direction, the grids attaching to the ground exhibited a vertical size of 0.05 mm and grow as a ratio of 1.1 until the vertical size reaches 2 mm. Besides, the uniform vertical distribution on this grid at a size of 2 mm is adopted, as illustrated in Fig. 2a. The total grid number is 8.3×10^6, ten times that of the grid number in the study by Liu and Ishihara (2015a,2015b).

2.3. Boundary conditions

The velocity profiles at the inlet are defined as:

$$\begin{cases} \tilde{u}_{rs} = U_1 \left(\dfrac{z}{z_1}\right)^{\frac{1}{n}} \\ \tilde{v}_{rs} = -\tilde{u}_{rs} tan(\theta) \end{cases} \tag{8}$$

where $\tilde{u}_{rs}$ and $\tilde{v}_{rs}$ denote radial velocity and tangential velocity at $r = r_s$, respectively; n is 7; the reference velocity U_1 and height z_1 are set as $0.24\ \mathrm{ms}^{-1}$ and 0.01 m, respectively, θ represents the inflow angle, that is variable to change S. At the outlet, the outflow boundary condition is used, where the gradients in pressure and velocities are set to zero. The boundary conditions are listed in Table 2.

$z^+ = \Delta z u_* / \upsilon$ as a function of radial distance for refined grids (the heights of the wall-attached grid are 1.0 mm, 0.3 mm, 0.15 mm and 0.1 mm in the refined mesh systems) are provided in Fig. 3. From Fig. 3 it is clear that for the finest grid system, z^+ is larger than 1 only in R6S4. The region $z^+ > 1$ is limited in $0.6 r_{\mathrm{vmax}} < r < 1.4\ r_{\mathrm{vmax}}$, where r_{vmax} is the radial distance of the location of the maximum tangential velocity. Further refining the mesh can hardly be afforded due to our limited computational resources. Considering the fact that the results of the finest mesh and the second finest mesh are almost same, we can say that the flow fields in tornado is not sensitive to z^+ if $z^+ < 2$, and 0.1 mm should be enough for the heights of wall-attached grid in the present LES. The summery of the numerical schemes is listed in Table 3.

2.4. Method changing Re

In the study by Monji (1985), the rich experimental data were provided. In order to do the direct and clear comparisons with experimental data by Monji (1985), we decided to use the same definition of Reynolds number as Monji (1985). Therefore, $2r_0$ and W_0 are taken as the representative length, $L^* = 2r_0$, and the representative velocity, $U^* = W_0$, respectively. Thus, Re is expressed as:

$$\mathrm{Re} = 2r_0 \cdot W_0 / \upsilon, \tag{9}$$

Where, $\upsilon = \mu/\rho$ denotes the kinematic viscosity. In the numerical simulation, the code solving the governing equations is in the dimensionless form normalized by L^* and U^*:

$$\frac{\partial \tilde{u}_i^*}{\partial t^*} + \frac{\partial \tilde{u}_i^* \tilde{u}_j^*}{\partial x_j^*} = \frac{1}{Re} \frac{\partial^2 \tilde{u}_i^*}{\partial x_j^* \partial x_j^*} - \frac{\partial \tilde{p}^*}{\partial x_i^*} - \frac{\partial \tau_{ij}^*}{\partial x_j^*}, \tag{10}$$

where, $\tilde{u}_i^* = \tilde{u}_i / W0\ x_i^* = x_i / 2r0$, and $t^* = tW0/2r0$. Thus, Re in the governing equation Eq. (10) can be easily changed. This method has been widely adopted to numerically examine the Reynolds effects in the other problems, including the studies by Min and Choi (1999) and Zeng et al. (2005).

However, if the Reynolds number is set to be sufficiently high, the SGS turbulent viscosity, μ_t, in LES will be significant, thus making the real Reynolds number of the modeled flow fields less than that from the setting. Accordingly, the significance of the SGS turbulent viscosity

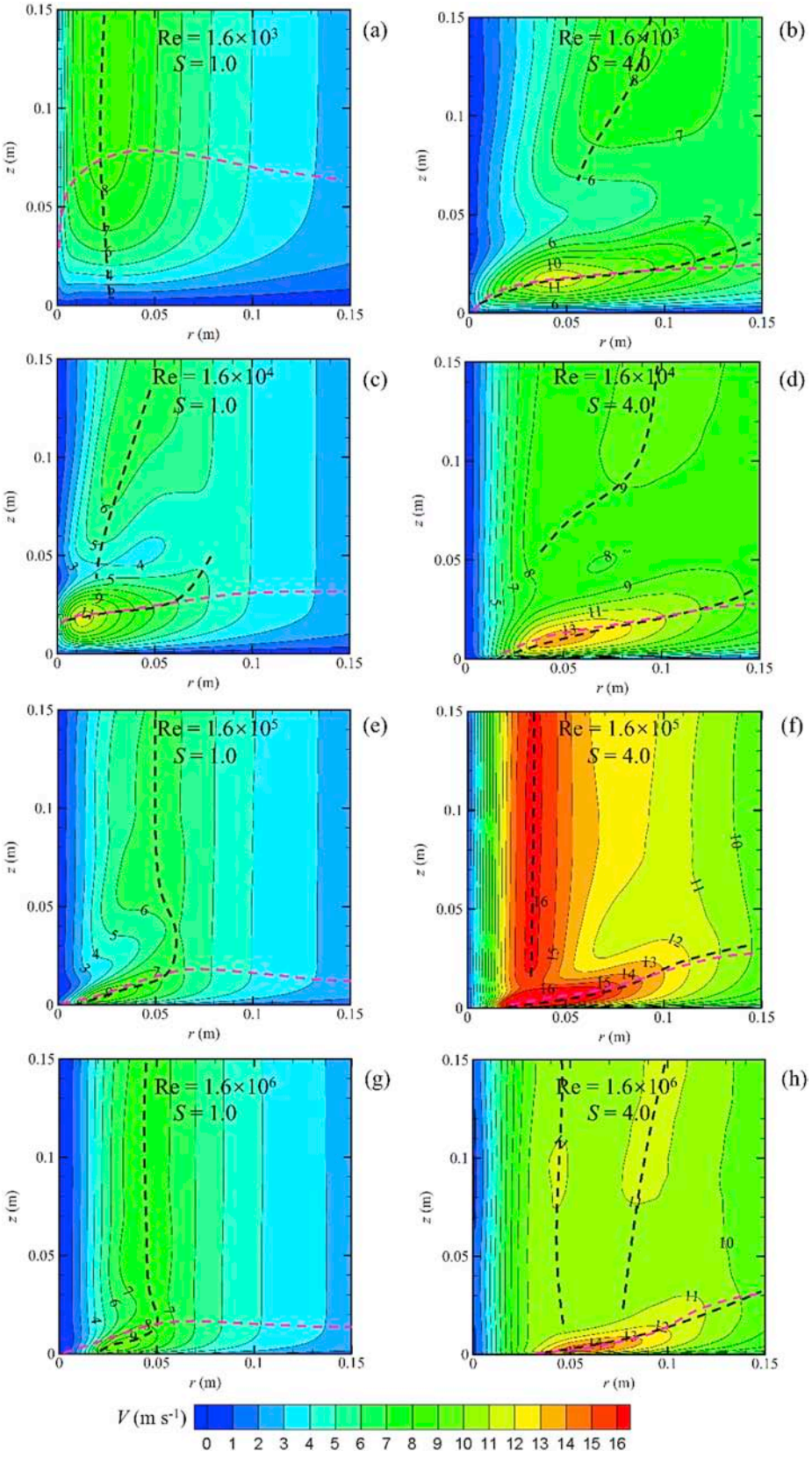

Fig. 10. Distributions of the time-space averaged tangential velocity on the vertical slice crossing the center of the tornado (a) R3S1, (b) R3S4, (c) R4S1, (d) R4S4, (e) R5S1, (f) R5S4, (g) R6S1, and (h) R6S4. The pink dashed lines show the depth of the convergence flow determined by the locations with 0.1 U_{max}, and the dark dashed lines indicate the locations the time-space averaged tangential velocity peaks. (For interpretation of the references to color in this figure legend, the reader is referred to the Web version of this article.)

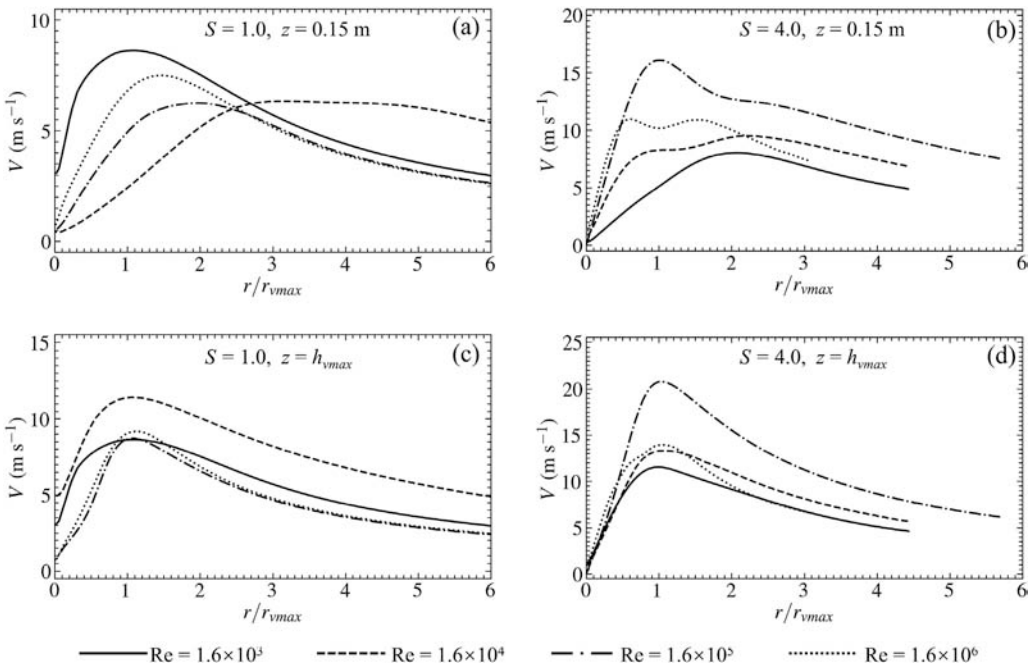

Fig. 11. Radial distribution of the time-space averaged tangential velocity for (a) $S = 1.0$ at $z = 0.15$ m, (b) $S = 4.0$ at $z = 0.15$ m, (c) $S = 1.0$ at $z = h_{\mathrm{vmax}}$, and (d) $S = 4.0$ at $z = h_{vmax}$.

model should be verified in advance.

The way to quantify the relative significance of the SGS turbulent viscosity is to compare it with that of the fluid viscosity. For the cases with the highest Re, μ_t is found to be only 5% of μ, suggesting that the decrease in Re due to the additional SGS turbulent viscosity is negligible.

2.5. Case settings

Eight cases with two swirl ratios $S = 1.0$ and 4.0, and four $\mathrm{Re} = 1.6 \times 10^3$, 1.6×10^4, 1.6×10^5, and 1.6×10^6, are considered, where the height at which the swirl ratios are evaluated is 0.05 m. The further increase in the Reynolds number will lead to significant increase of SGS viscosity, thereby significantly decrease the real Reynolds number of the fluids. The way to reduce the importance of SGS viscosity is to refine the grid, which is however not affordable based on the computational capability of the authors, therefore $\mathrm{Re} = 1.6 \times 10^6$ becomes the upper limitation of our tornado simulations. The case settings are summarized in Table 4, where the h_{vmax} is the height at which the maximum tangential velocity, $V_{\max}$, occurs.

3. Results and discussions

3.1. Instantaneous flow fields

The instantaneous flow fields are illustrated to present a general image of the characteristics in the tornados. The technology of Q-criterion is employed to visualize the flow fields. Q quantifies the relative amplitude of the rotation rate and the strain rate of the flow.

$$Q = 1/2\left(S_{ij}S_{ij} - \Omega_{ij}\Omega_{ij}\right), \tag{11}$$

where $S_{ij} = 1/2(\partial\tilde{u}_i/\partial x_j - \partial\tilde{u}_j/\partial x_i)$ and $\Omega_{ij} = 1/2(\partial\tilde{u}_i/\partial x_j + \partial\tilde{u}_j/\partial x_i)$ denote the antisymmetric and symmetric components of the velocity-gradient tensor, respectively, of the velocity-gradient tensor. Therefore, S_{ij} and Ω_{ij} represent shear strain and rotation of the flow, respectively.

Fig. 4 gives the three-dimensional view of the flow in the tornado-like vortices. When $S = 1.0$, two iso-surfaces with $Q = 20000$ s^{-2} and $Q = -20000$ s^{-2} are plotted; when $S = 4.0$, two iso-surfaces with $Q = 50000$ s^{-2} and $Q = -50000$ s^{-2} are drawn. The iso-surfaces of Q values are further colored by the instantaneous tangential velocities.

For $S = 1.0$, the vortex attributed to the flow rotation does not break into the turbulence eddies in R3S1 (Fig. 4a) whose Q iso-surfaces exhibit a cup-shape. Note that the Q iso-surfaces exhibit some wavy-spiral structures, which should be attributed to the fact that in the very center of the core, the vertical and tangential velocities are large, providing large velocity shear at the boundary of the tornado core. With the rise in Re, the viscous force of the fluids turns smaller than the inertial ones. As a result, failing to hold the clear wavy-spiral structure, the fluids break into eddies with smaller sizes. Notably, the wavy-spiral structure is clearly observed at the very beginning when R4S1 was being modeled (Fig. 4c), whereas this wavy-spiral structure suddenly broke as the modeling advanced. In addition, there exist an interesting phenomenon in R4S1. In the core region close to the ground, identification of the wavy-spiral structure remains possible, suggesting that the flow close to the ground for R4S1 is similar to that of R3S1 at the low elevation. Increasing Re to R5S1 (Fig. 4e), the wavy-spiral structure close to the ground found in R4S1 vanishes.

When $S = 4.0$, the single-celled vortex found at $S = 1.0$ cannot be observed even under the lowest Reynolds number $\mathrm{Re} = 1.6 \times 10^3$. However, similar to R4S1, the turbulent flow fields of R3S4 are characterized by some elongated streaky structures surrounding the major core of the tornado, as presented in Fig. 4b. These elongated eddies further break into small vortices as increasing Re to R4S4 (Fig. 4d), R5S4 (Fig. 4f) and R6S4 (Fig. 4h), respectively. In the very central part of tornado core, the flow is calm, covering larger area with larger Re.

The overall view of the turbulence structures can be well presented by Q iso-surfaces; whereas the flow at the inner part of the tornados is difficult to present. Therefore, the distributions of Q on a vertical slice passing through the tornado simulator center, and on a horizontal slice passing through $z = 0.15$ m, are also plotted as shown in Fig. 5 and Fig. 6, respectively.

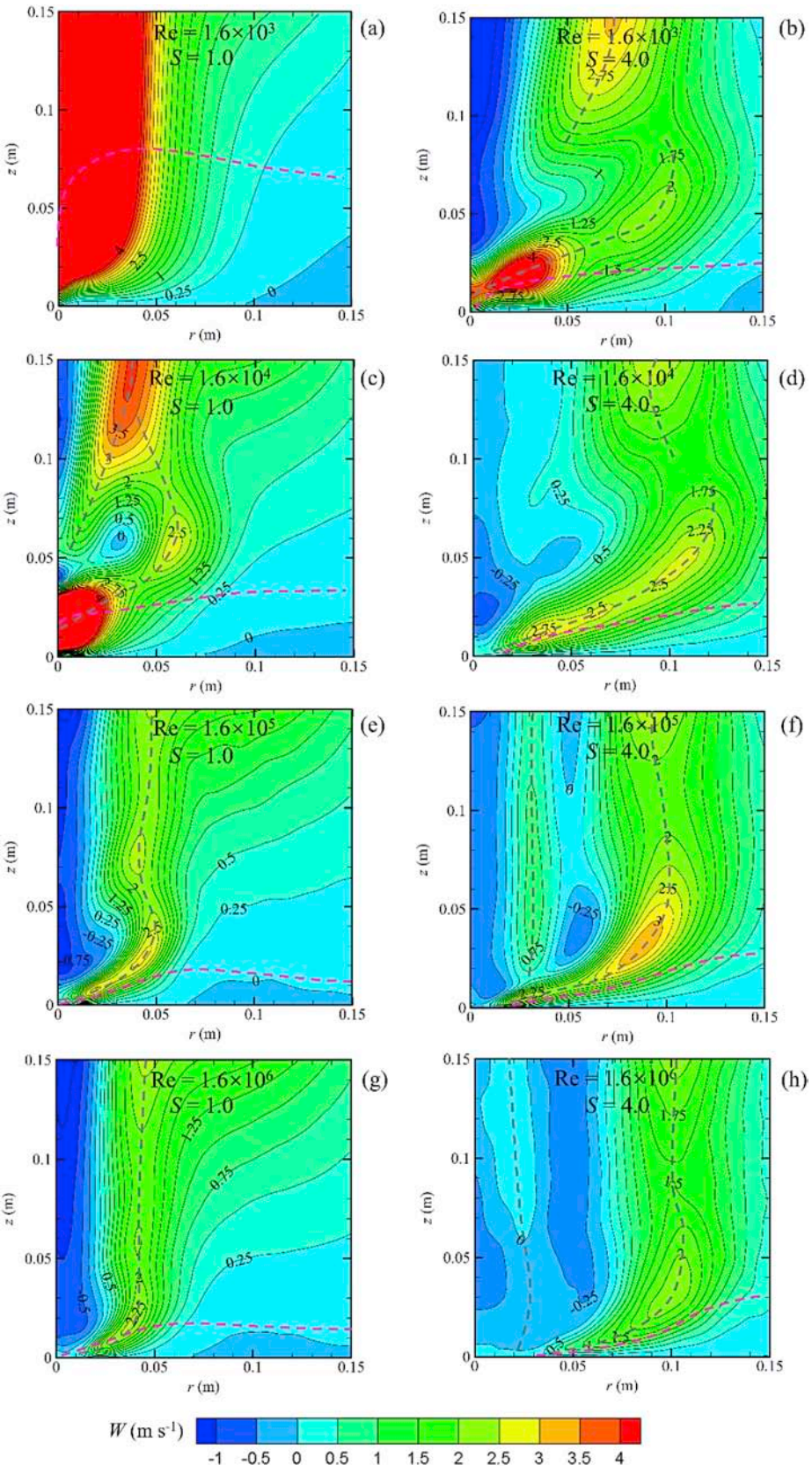

Fig. 12. Distributions of the time-space averaged vertical velocity on the vertical slice crossing the center of the tornado (a) R3S1, (b) R3S4, (c) R4S1, (d) R4S4, (e) R5S1, (f) R5S4, (g) R6S1, and (h) R6S4. The pink dashed lines show the depth of the convergence flow determined by the locations with 0.1 U_{max}, and the grey dashed lines indicate the locations the time-space averaged vertical velocity peaks. (For interpretation of the references to color in this figure legend, the reader is referred to the Web version of this article.)

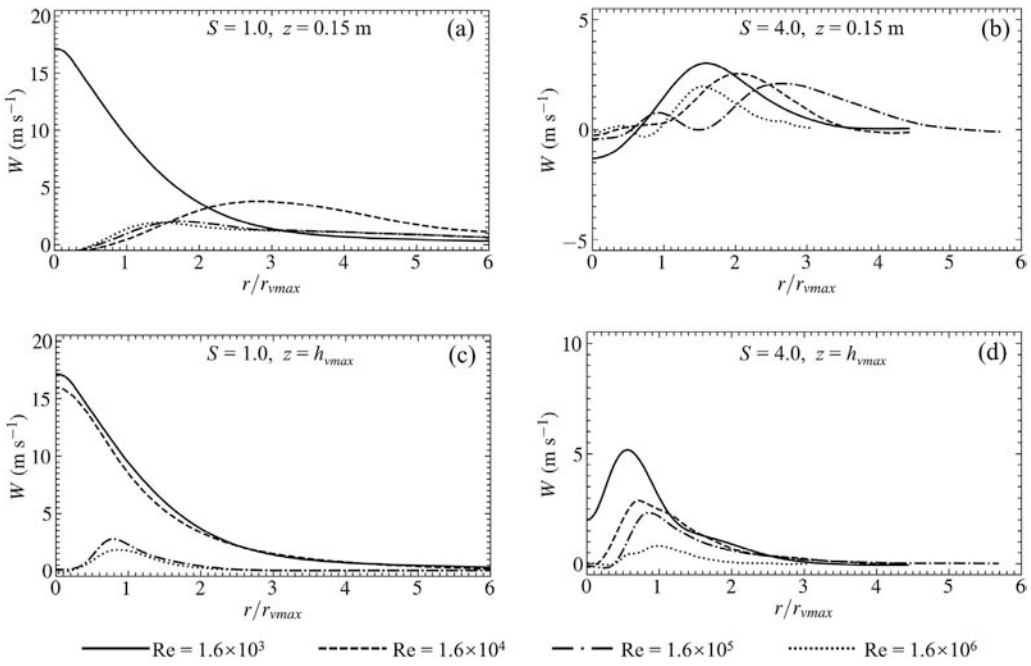

Fig. 13. Radial distribution of the time-space averaged vertical velocity for (a) $S = 1.0$ at $z = 0.15$ m, (b) $S = 4.0$ at $z = 0.15$ m, (c) $S = 1.0$ at $z = h_{vmax}$, and (d) $S = 4.0$ at $z = h_{vmax}$.

Fig. 5 (a) displays positive Q in the center and negative Q at the corner of R3S1. Increasing Re to R4S1 (Fig. 5c), Q close to the ground exhibits similar distributions with that of R3S1. Nevertheless, this similarity only maintains up to $z = 0.04$ m, above which the positive and negative Q are mixed. From the later discussion of the turbulence statistics, the vertical velocity of R4S1 tornado is found to be much large significantly close to the ground. However, it suddenly decreases to nearly zero, and thus a stagnation point is formed, dividing the flow in R4S1 into two regions: one-celled tornado close to the ground and two-celled tornado above the stagnation point. Increasing Re to R5S1 (Fig. 5e) and R6S1 (Fig. 5g), the stagnation point moves upstream and touches the ground. Stopped by such touch-down stagnation point, the convergence flow close to the ground then moves upward and outward. The sudden change in the direction of the convergence flow near the ground generates large flow shear, and then much turbulence around the corner is generated.

Under high $S = 4.0$, when $\mathrm{Re} = 1.6 \times 10^3$, the similar flow structure as R4S1 can be found, as illustrated in Fig. 5b. Further increasing Re to R4S4 (Fig. 5d), the near-ground convergence flow cannot meet at the tornado center, whereas it gets stopped by a stagnation ring due to the further upstream motion of the stagnation point. Moreover, the funnel shape found in R3S4 almost disappears. More obvious near-corner outward motion of the convergence flow is observed with Re rising to R5S4 (Fig. 5f) and R6S4 (Fig. 5h).

The sub-vortex and the "swaths" in the tornadoes are found and shown in a clearer manner on the slice of $z = 0.15$ m, as shown in Fig. 6, where the sub-vortex and the "swaths" around the tornado core are presented by dashed circles and solid lines, respectively. It is clear that the sub-vortex can only appears in the central calm flow region. Obviously, three sub-vortices can be identified in R5S1 and R6S1, and about five swaths in R5S4.

3.2. Mean velocities

The mean vectors on the vertical slice crossing the center of the tornado simulator are shown in Fig. 7. The dashed lines superimposed on Fig. 7 represent the depth of the convergence flow, d_c, connecting the locations with one tenth of the maximum radial velocity, $U_{\max}$. It can be identified that for all the cases except for the single-celled vortex R3S1, the maximum vertical velocity, $W_{\max}$, shows a growing trend as Re increases. It is noteworthy that the vectors plotted in this study are based on the time-azimuthal averaged flow fields. If the flow fields are only averaged in time, the inner radial velocity will hardly be zero, especially in the cases R5S1 (Fig. 7e) and R6S1 (Fig. 7g), which may be explained by the unstable stagnation point at this stage, as has been discussed in detail by Ashton et al. (2019). Furthermore, lower d_c is found with the rise in Re or S. However, in the outer region of the tornado, d_c is found to be only controlled by S.

The distribution of the time and spacing averaged radial velocity, $U = \langle \tilde{u} \rangle$, is shown in Fig. 8, where the negative and positive U represents inward and outward motions of the flow respectively. For $S = 1.0$, the maximum outward radial velocity reaches $4\ \mathrm{m\,s^{-1}}$ at $\mathrm{Re} = 1.6 \times 10^5$. Since the outward radial velocity is primarily caused by the direction variation of the inward flow close to the ground and that the sum of the mass flux should be zero, the outward radial velocity should experience a decrease due to the expansion of the tornado with the increase in Re, i.e., $4\ \mathrm{m\,s^{-1}}$ at R4S1 (Fig.8 c), $1\ \mathrm{m\ s^{-1}}$ at R5S1 (Figs. 8 e) and $0.8\ \mathrm{m\,s^{-1}}$ at R6S1 (Fig. 8 g). In addition, the area covered by positive radial velocity shows an ellipse shape with major axis tilted; the angle between the ellipse major axis and the x axis tends to be a constant scatting around 20°. The maximum inward radial velocity is found not sensitive to Re after the vortex core breaks, which are all about $6.5\ \mathrm{m\,s^{-1}}$ in the cases of R4S1 (Fig. 8 c), R5S1 (Fig. 8 e) and R6S1 (Fig. 8 g). However, due to the upstream motion of the stagnation point, the layer with inward radial velocity is compressed for larger Re.

At $S = 4.0$, the features found in the low swirl cases remain true. On the one hand, the maximum inward radial velocity is nearly constant, reaching about $8\ \mathrm{m\ s^{-1}}$. On the other hand, the layer with inward radial velocity becomes thinner with the increase in Re. In addition, the sensitivity of the maximum outward radial velocity to Re found in the low swirling cases still holds for the high swirl cases, in which it decreases from $4.5\ \mathrm{m\,s^{-1}}$ in R3S4 (Fig. 8 b) to about $1.5\ \mathrm{m\,s^{-1}}$ in R6S4 (Fig. 8 h). However, the ellipse shape of the area with positive radial velocity is distorted as Re increases to 1.6×10^5. By connecting the locations of the peak positive radial velocities, the curve is not a straight line anymore, revealing the more difficult penetration of the convergence flow to the corner of the tornado for larger Re.

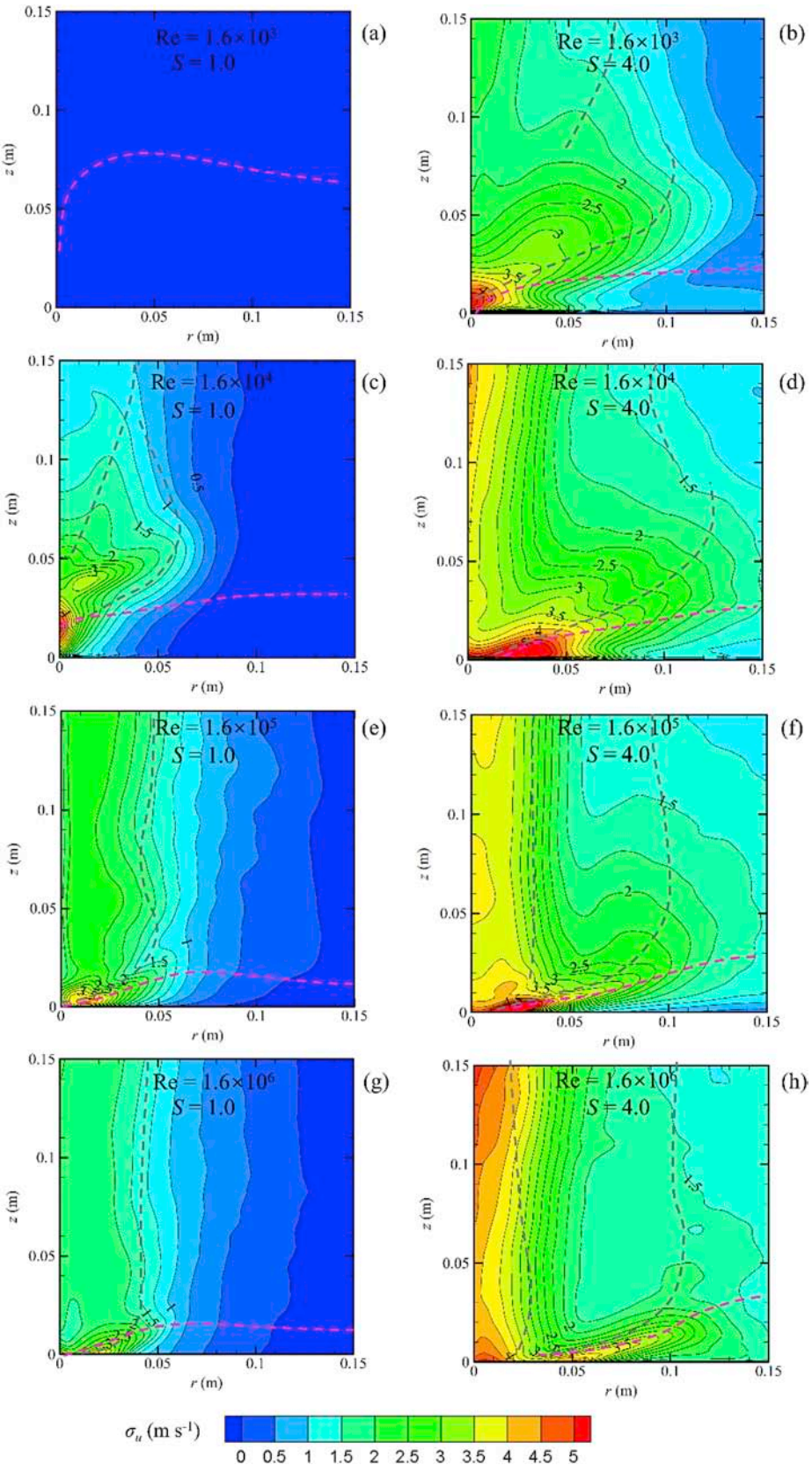

Fig. 14. Distributions of the space averaged r.m.s. of the fluctuations of the radial velocity on the vertical slice crossing the center of the tornado (a) R3S1, (b) R3S4, (c) R4S1, (d) R4S4, (e) R5S1, (f) R5S4, (g) R6S1, and (h) R6S4. The pink dashed lines show the depth of the convergence flow determined by the locations with 0.1 U_{max}, and the grey dashed lines indicate the locations the time-space averaged vertical velocity peaks. (For interpretation of the references to color in this figure legend, the reader is referred to the Web version of this article.)

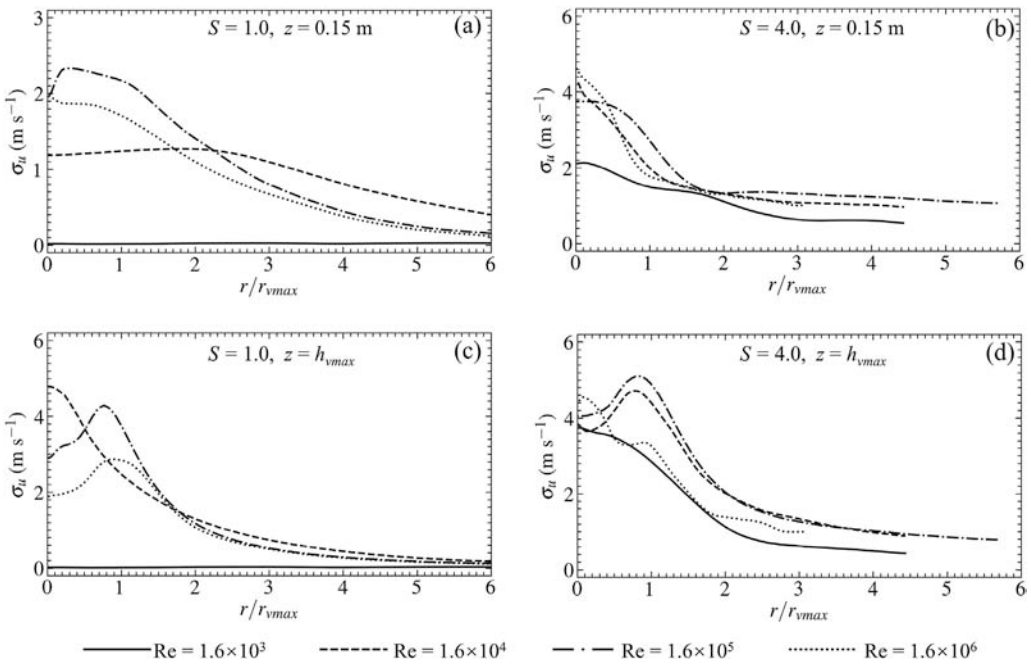

Fig. 15. Radial distribution of the space averaged r.m.s. of the fluctuation of radial velocity for (a) $S = 1.0$ at $z = 0.15$ m, (b) $S = 4.0$ at $z = 0.15$ m, (c) $S = 1.0$ at $z = h_{vmax}$, (d) $S = 4.0$ at $z = h_{vmax}$.

The radial profiles of U are shown in Fig. 9 in a more quantitative manner. Two elevations are selected, with one at $z = 0.15$ m, which can be considered as the cyclostrophic balance region, i.e., the centrifugal force balances with the pressure gradient forces, and the other h_{vmax}. The height with maximum tangential velocity is selected given that the tangential velocity is the major component in the tornado-like vortices [Kuai et al. (2008) and Hangan and Kim (2008)]. At h_{vmax}, the negative radial velocity is strengthened for all of the cases. Furthermore, the location of the peak positive radial velocity moves outward with increasing Re.

Fig. 10 illustrates the distribution of mean tangential velocity, $V = \langle\tilde{v}\rangle$. Except the single-celled vortex R3S1, the maximum tangential velocity, $V_{\max}$, in all of the cases occurs at the corner of the tornadoes and gets larger with the increase in S. However, $V_{\max}$ does not show large variations as a function of Re. The flow in R4S1 (Fig. 10 c) is a typical transitional stage from the single-celled vortex to the two-celled vortex, as discussed in detail by Liu et al. (2018). From Fig. 10f, R5S4 seems to be also a transitional stage to the multi-celled vortex. For one thing, $V_{\max}$ is the largest for R5S4; for another, in the cyclostrophic balance region, the mean tangential velocity peaks in a very narrow region compared with the other three cases at $S = 4.0$. In addition, according to the plotting of Q values, obvious "swaths" are only identified in R5S4. At $z = h_{vmax}$ the tangential velocity peaks at almost the same radial locations, as suggested from the illustration of the radial profiles of V in Fig. 11. Interestingly, at $z = 0.15$ m, two peaks on the radial profiles of tangential velocity can be identified at R4S4 and R6S4.

The strong acceleration of the mean vertical velocity, $W = \langle\tilde{w}\rangle$, is found at the central core of R3S1 (Fig. 12a) and the near ground corner of R4S1 (Fig. 12c). The magnitudes of the maximum vertical velocity, $W_{\max}$, in R3S1 and R4S1 are almost the same, nearly 16 m s^{-1}. After the tornado reaching the stages after vortex breakdown, the near corner peak vertical velocity is approximately a constant scatting about 2.5 m s^{-1}. Moreover, the negative vertical velocity seems only occur at the high swirl cases, and with abruptly a constant -0.5 m s^{-1}.

The plotting of the radial profiles of W reveals that the locations of the peak W at both $z = 0.15$ m and $z = h_{vmax}$ move outward slightly with the increase in Re, but this expansion is limited especially for the stages safely after the vortex breakdown stage, as shown in Fig. 13.

3.3. Fluctuations

The wandering motion of the tornado core has been observed in the studies by Ishihara and Liu (2014), Liu et al. (2018), and Ashton (2019). Due to this wandering motion, the center the simulator will experience large and small velocities periodically, generating large fluctuations of the velocities. If we can find the tornado center at each time step and translate the numerical data to the coordinate determined by the tornado center instead of the simulator center, it is possible to calculate the mean velocities as well as the root mean square (r.m.s.) of the velocities respect to the tornado center. However, the distance from the tornado center to the simulator center is not a constant at each time step and at each elevation. It is also difficult to determine the tornado center in the instantaneous flow fields. In addition, using the fixed coordinate determined by the tornado simulator is also from the consideration that, in the real application of wind engineering, the wind-resistant structures are fixed. The wind-resistant structures can experience the large fluctuations of the velocities due to the wandering motion of the tornado. This large fluctuation of the wind is important to evaluate the dynamic response of the structure. If the properties of the wandering motion of the tornado can be clarified, it will be possible to find a relationship between the turbulence statistics determined using these two coordinates, which will be helpful for building the tornado flow field model. In the future, this issue will be studied. In the present study, we decided to use the traditional method and the fixed coordinate to determine the turbulence statistics, just like the study by Tari et al. (2010).

Root mean square of the velocity fluctuations based on the fixed coordinate is defined as $u_i = \sqrt{\sum(\tilde{u}_i - \langle\tilde{u}_i\rangle)^2/n}$. The radial velocity fluctuation u is depicted in Fig. 14 using contours and Fig. 15 using profiles. Except for the single-celled tornado R3S1 (Fig. 14a), the radial velocity fluctuations exhibit about the same level at a certain swirl ratio. In the cases of $S = 1.0$ and $S = 4.0$, the maximum radial velocity fluctuation, $u_{\max}$, scatters around 3 m s^{-1} and 4.5 m s^{-1}, respectively. Similar distribution of u in between R4S1 (Fig. 14c) and R3S4 (Fig. 14b) is found. As increasing Re, two regions with large u (one is in the central core of the tornadoes; the other is near the ground whose location almost coincides with that of the inversion point of U) are clearly identified in R5S1, R6S1, R4S4, R5S4 and R6S4.

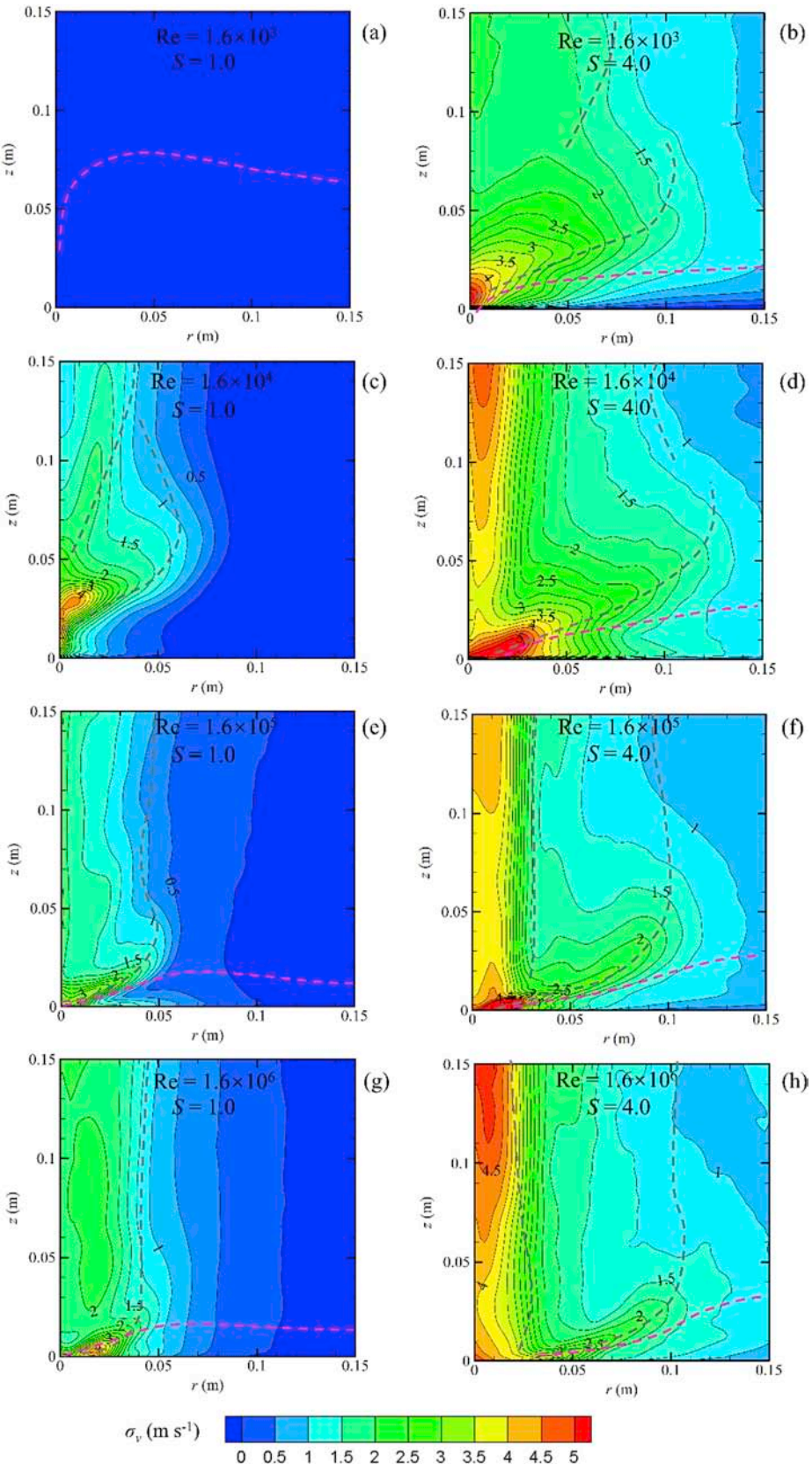

Fig. 16. Distributions of the space averaged r.m.s. of the fluctuations of the tangential velocity on the vertical slice crossing the center of the tornado (a) R3S1, (b) R3S4, (c) R4S1, (d) R4S4, (e) R5S1, (f) R5S4, (g) R6S1, and (h) R6S4. The pink dashed lines show the depth of the convergence flow determined by the locations with 0.1 U_{max}, and the grey dashed lines indicate the locations the time-space averaged vertical velocity peaks. (For interpretation of the references to color in this figure legend, the reader is referred to the Web version of this article.)

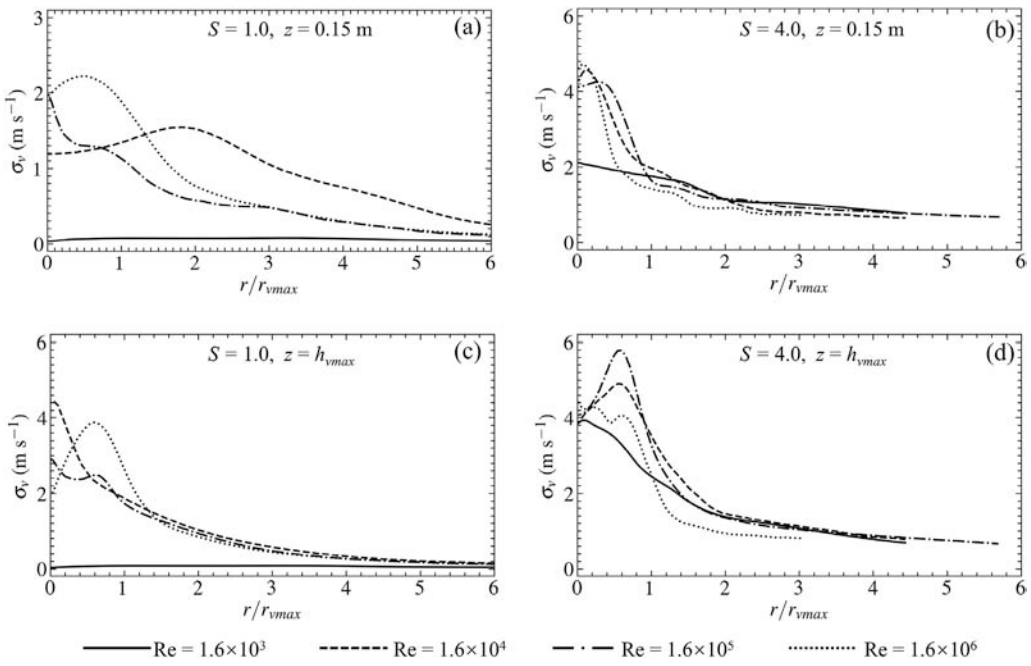

Fig. 17. Radial distribution of the space averaged r.m.s. of the fluctuation of tangential velocity for (a) $S = 1.0$ at $z = 0.15$ m, (b) $S = 4.0$ at $z = 0.15$ m, (c) $S = 1.0$ at $z = h_{vmax}$, (d) $S = 4.0$ at $z = h_{vmax}$.

The distributions of tangential velocity fluctuation v are similar with those of u, as shown in Fig. 16 and Fig. 17. Most interestingly, at $r = 0$, u equals to v, probably due to the unstableness of the tornado core moving around the center of the simulator. This organized wandering of the tornado core yields nearly the sinusoidal curve with the same amplitude and period for $\tilde{u}$ and $\tilde{v}$, as discussed by Ashton et al. (2019). Therefore, in the present LES, the same value of u and v further confirms that the organized wandering of the tornado core will occur no matter how large Re is.

Figs. 18 and 19 show the distribution of the vertical velocity fluctuation, w. For $S = 1.0$, w at $z = 0.15$ is peaked at about $r = 0.015$ m, except the single-celled tornado R3S1. This trend still holds for higher Reynolds number cases R5S1 and R6S1 as suggested in Fig. 18e, g. Interestingly, at $S = 4.0$, almost the same peak values of w in the cyclostrophic balance region are found for different Reynolds numbers. However, the situation becomes complicated for $z = h_{vmax}$. Firstly, the same peaks found in the cyclostrophic balance region are not preserved at $z = h_{vmax}$. Secondly, at $z = h_{vmax}$, additional regions with high w can be identified at about $r = 0.02$ m for R4S4 (Fig. 18 d) and R5S4 (Fig. 18 f). In addition, nearly zero w is observed for R6S4 (Fig. 18 h). Importantly, extraordinary energetic vertical fluctuations in R4S1 (Fig. 18 c) and R3S4 (Fig. 18 b) locating at around the stagnation point can be clearly identified. In fact, the mechanism of the peak w for R4S1 and R3S4 (near vortex breakdown stage) is different from that of R5S1, R6S1, R4S4, R5S4, and R6S4 (safely after vortex breakdown stage). The major contribution of the large w for the former two cases is from the vertical vibration of the unstable vortex bubble; while that of the latter cases results from the horizontal vibration of the tornado core and the large wind shear.

3.4. Skewness and kurtosis

PDF of the fluctuating velocities is vital to the examination of the gust wind in the tornado-like vortices, which is also important for the evaluation of tornado-induced dynamic loads on structures. Skewness and kurtosis are applied in the present study to examine the PDF shape of the fluctuating velocities, the skewness of u_i is expressed as:

$$Sk_{u_i} = u_i^{'3} \Big/ u_i^{'3/2}, \tag{12}$$

which indicates the symmetry of PDF of u_i. It is noteworthy that the skewness of any univariate normal distribution is 0. Also, the kurtosis of u_i is formulated as:

$$Ku_{u_i} = u_i^{'4} \Big/ u_i^{'2}, \tag{13}$$

Which denotes the peakedness of the sampled events. Note that the kurtosis of any normal distribution is 3. Furthermore, the kurtosis should never be less than 1 but reach 1.8 once the PDF is uniform. In the following discussion about skewness and kurtosis, the data of the tangential velocity will be provided.

Since skewness and kurtosis require higher order terms in the expressions, their distributions become not as smooth as those of mean velocities and the fluctuations, as shown in Fig. 20 and Fig. 21. At $S = 1.0$, particularly large Sk_v are found in R3S1 (Fig. 20a) due to the almost zero fluctuation in the flow fields. Increasing Re to R4S1 (Fig. 20c), much large negative Sk_v is found at the boundary of the vortex bubble in R4S1, and the area with negative Sk_v experiences a shrink with increasing Re as observed in R5S1 (Fig. 20e) and R6S1 (Fig. 20g).

However, for the cases with $S = 4.0$, the area with negative Sk_v in the near corner region becomes much smaller compared with those with $S = 1.0$. Moreover, for all the cases after the vortex breakdown stage, Sk_v decreases significantly as the flow moves to the tornado center, and almost reaches zero at $r = 0$.

The kurtosis of the tangential velocity forms a similar shape with the skewness (Fig. 21). Except R3S1 and R4S1, in most of the regions, Ku_v scatters around 3. When moving to the center of the tornado, Ku_v decreases close to 1.8, implying a uniform distribution of PDF. In addition, the negative Sk_v and Ku_v primarily locate at the place where W reaches its peak values.

3.5. Momentum and turbulent kinetic energy budget

The momentum budget is useful to understand the major contribution in the force balance of the fluids and can be further applied to simplify

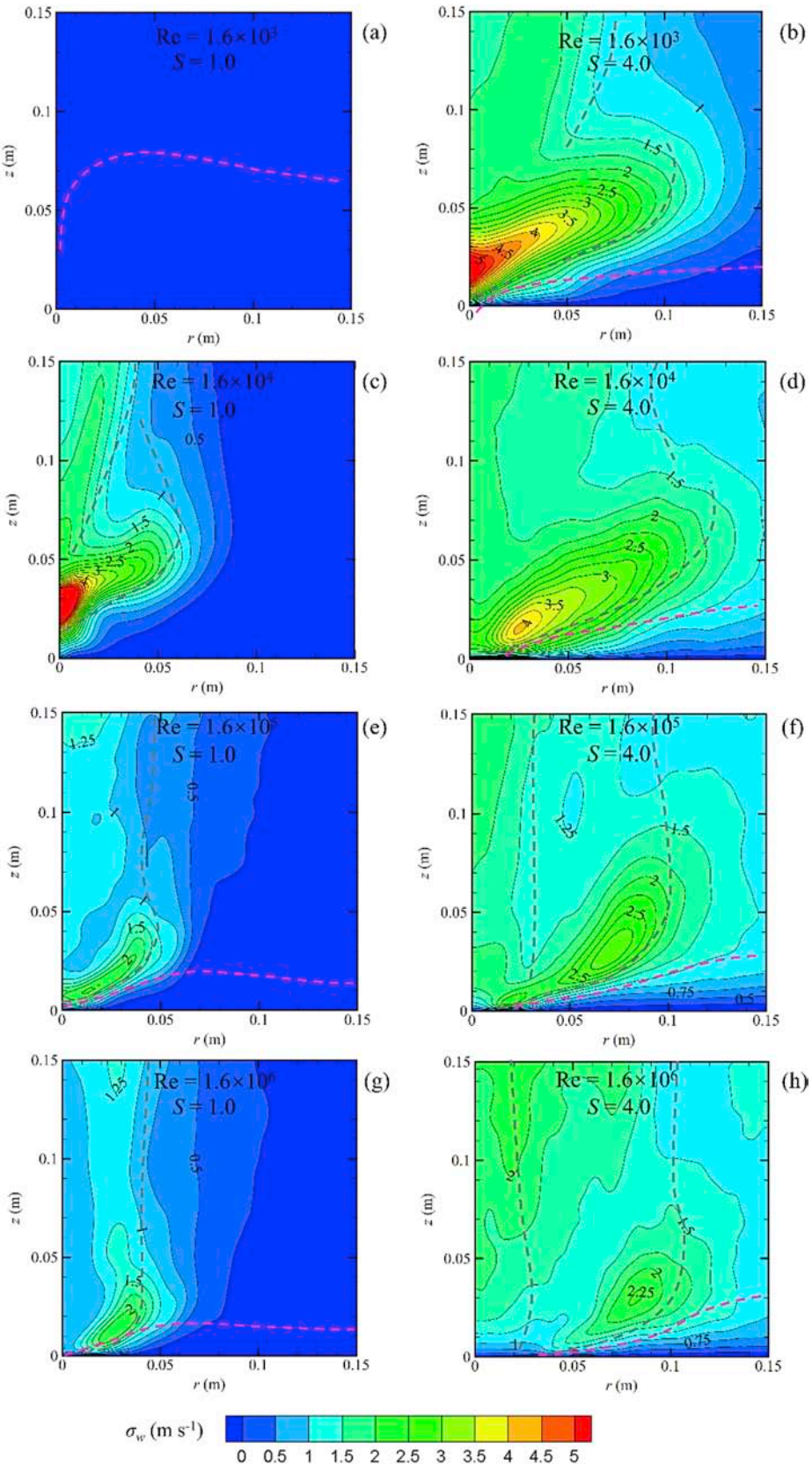

Fig. 18. Distributions of the space averaged r.m.s. of the fluctuations of the vertical velocity on the vertical slice crossing the center of the tornado (a) R3S1, (b) R3S4, (c) R4S1, (d) R4S4, (e) R5S1, (f) R5S4, (g) R6S1, and (h) R6S4. The pink dashed lines show the depth of the convergence flow determined by the locations with 0.1 U_{max}, and the grey dashed lines indicate the locations the time-space averaged vertical velocity peaks. (For interpretation of the references to color in this figure legend, the reader is referred to the Web version of this article.)

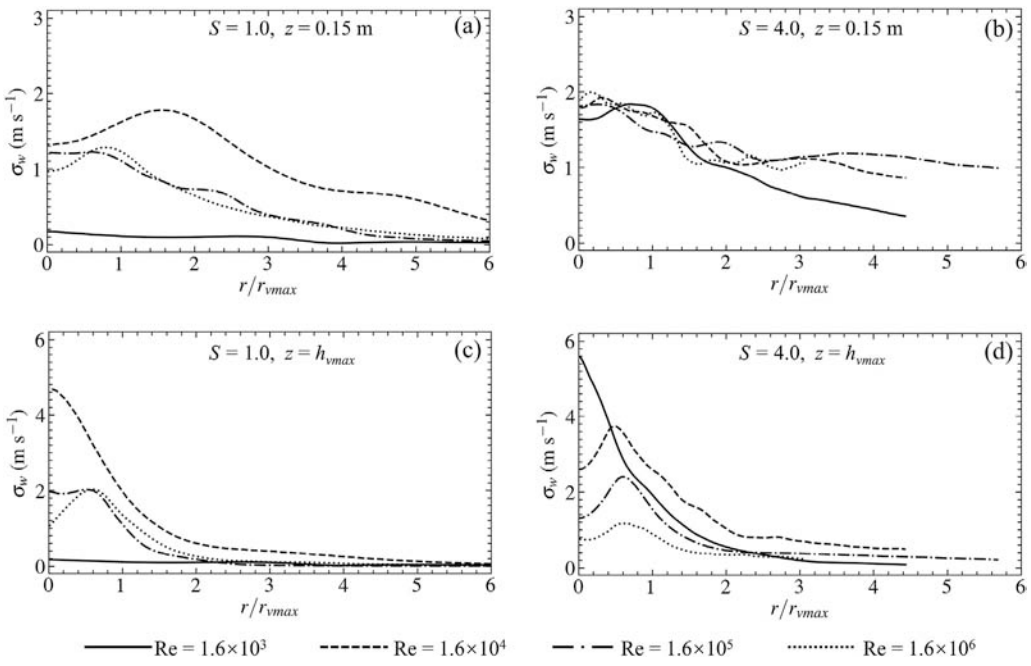

Fig. 19. Radial distribution of the space averaged r.m.s. of the fluctuation of vertical velocity for (a) $S = 1.0$ at $z = 0.15$ m, (b) $S = 4.0$ at $z = 0.15$ m, (c) $S = 1.0$ at $z = h_{vmax}$, (d) $S = 4.0$ at $z = h_{vmax}$.

the governing equations, making it possible to provide an analytical model of the mean flow fields. The momentum budget of the Reynolds averaged flow fields in the cylindrical coordinates in radial direction can be formulated as:

$$U\frac{\partial U}{\partial r} + W\frac{\partial U}{\partial z} - \frac{V^2}{r} = -\frac{1}{\rho}\frac{\partial P}{\partial r} - T_u + D_u, \tag{14}$$

The left-hand side consists of the radial advection A_{ru}, the vertical advection A_{zu} and the centrifugal force C_r; the right-hand side includes the radial pressure gradient P_r, turbulent force T_u and diffusion D_u. In the cyclostrophic balance region, the momentum balance is just in between the radial pressure gradient and the centrifugal force; hence, only the momentum budget at h_{vmax} is provided as shown in Fig. 22.

For $S = 1.0$, at the single-celled vortex stage R3S1 (Fig. 22 a), the major balance is almost in between P_r and C_r. As increasing Re to R4S1 (Fig. 22 c), the contribution from A_{zu} becomes stronger; while at R5S1 (Fig. 22 e), A_{zu} is even larger than P_r. Further increasing Re to R6S1 (Fig. 22 g), A_{zu} decreases and the major balance appears again in between C_r and P_r.

The trend of the cases $S = 4.0$ is similar to that of the cases $S = 1.0$. At low Re (R3S4, R4S4, in Fig. 22 b, d, respectively), C_r, P_r and A_{zu} indicate the main balance. However, when Re is sufficiently high (R5S4, R6S4, in Fig. 22 f, h, respectively), the contribution from A_{zu} almost disappears, suggesting the similar distribution to that found in the cyclostrophic balance region.

The wall shear will directly affect the advection terms in the momentum balance. And from the plotting of the momentum balance, it is clear that the advection term A_{zu} is much stronger than A_{ru}. Therefore, the ratio between the advection term A_{zu} to the centrifugal term C_r is calculated and plotted in Fig. 23. It can be found that the wall shear is important for the tornado with small swirl ratios, as increasing the swirl ratio, the wall shear become less important. In addition, increasing the Reynolds number will also shrink the region with large wall shear effects. For the cases R6S1, R5S4, and R6S4, the region with obvious wall shear effects almost dismisses. Therefore, it is safe to state that when the swirl ratio or the Reynolds number is sufficiently high, the major balance between the radial pressure gradient and the centrifugal force will be reached balance, expressed as:

$$\frac{V^2}{r} = \frac{1}{\rho}\frac{\partial P}{\partial r}, \tag{15}$$

3.6. Similarity parameter

Monji (1985) plotted the variations of the vortex type as a function of Re and S. Furthermore, the curve of Re versus S for each type of the vortex was found to follow an exponential function. The exponent of the function increases as the tornado changes from one-celled type to the multi-celled type. In addition, as has been observed by Fiedler (2009), the effects of S on the tornado-like flow fields are comparable to those of $\mathrm{Re}^{-1/3}$. Therefore, the types of the tornado-like vortex plotted in Monji (1985) are re-plotted together with the simulated tornadoes in the present LES and the data in the study by Matsui and Tamura (2009) as a function of $\mathrm{Re}^{-1/3}$ (x axis) and S (y axis) in Fig. 24, where the solid straight lines are the curves fitting the types of tornadoes adapted from the plotting in Monji (1985). It can be clearly found that, the relationship between $\mathrm{Re}^{-1/3}$ and S in each group of the tornadoes almost follows the expression:

$$S = a + b\,\mathrm{Re}^{-1/3}, \tag{16}$$

Where, the constant a and the slope b tend to be increased as the tornado changes from one-celled type to multi-celled type. From the above discussion of the present LES, R3S1 has been found to be a single-celled tornado, R4S1 and R3S4 are found to be the transitional ones, R5S1, R6S1, and R4S4 are the tornadoes with about three sub-vorices, and R5S4 and R6S4 are multi-celled ones, showing the similar trend with that by Monji (1985). The discrepancies may result from the different configurations of the tornado simulators. Some non-linear trends in R5S4 and R6S4 should be the indication that the S(Re) relationship is limited to a narrow Reynolds range. Choosing the popper scaling may remove the

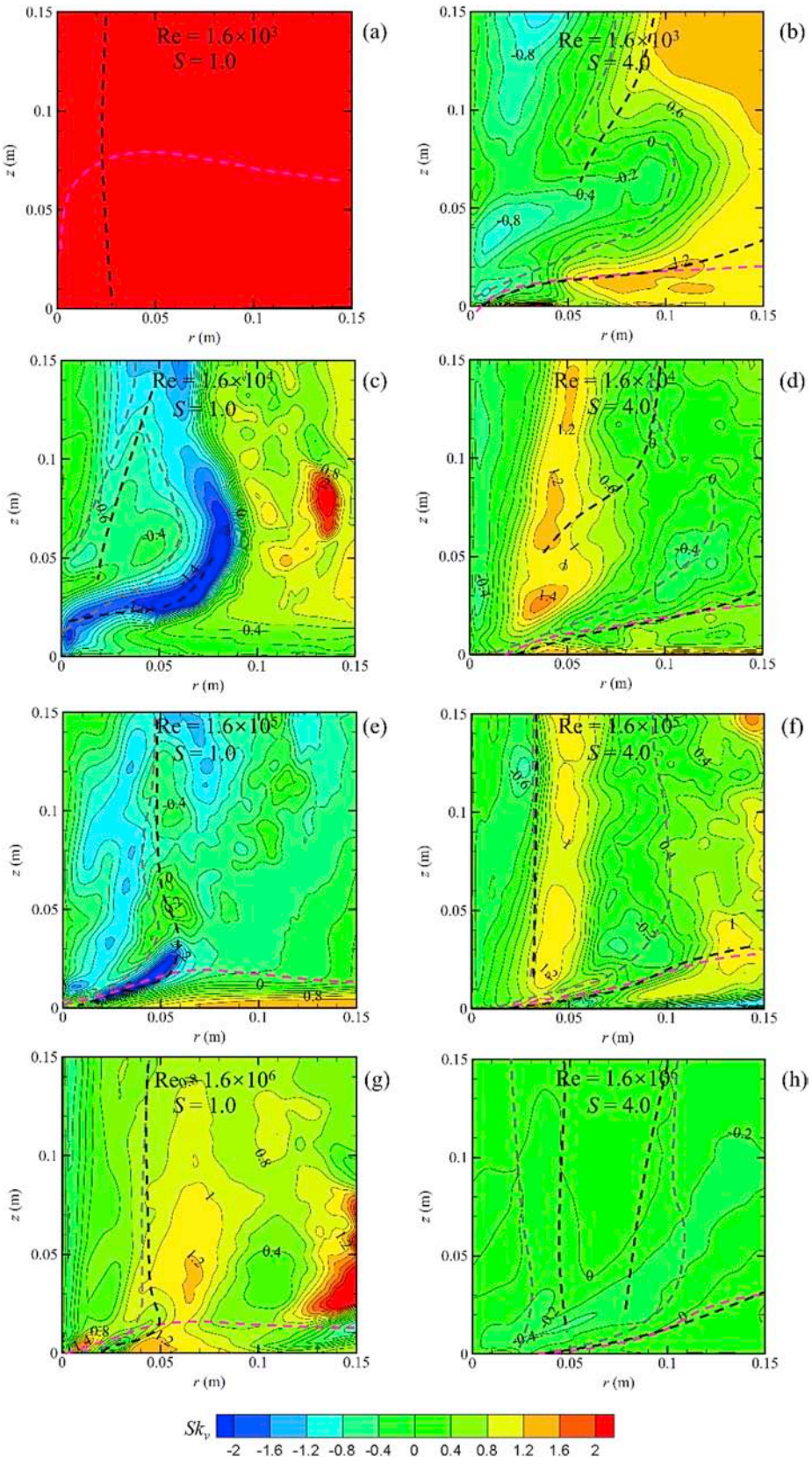

Fig. 20. Distributions of the space averaged skewness of the tangential velocity on the vertical slice crossing the center of the tornado (a) R3S1, (b) R3S4, (c) R4S1, (d) R4S4, (e) R5S1, (f) R5S4, (g) R6S1, and (h) R6S4. The pink dashed lines show the depth of the convergence flow determined by the locations with 0.1 U_{max}, the dark dashed lines indicate the locations the time-space averaged tangential velocity peaks, and the grey dashed lines indicate the locations the time-space averaged vertical velocity peaks. (For interpretation of the references to color in this figure legend, the reader is referred to the Web version of this article.)

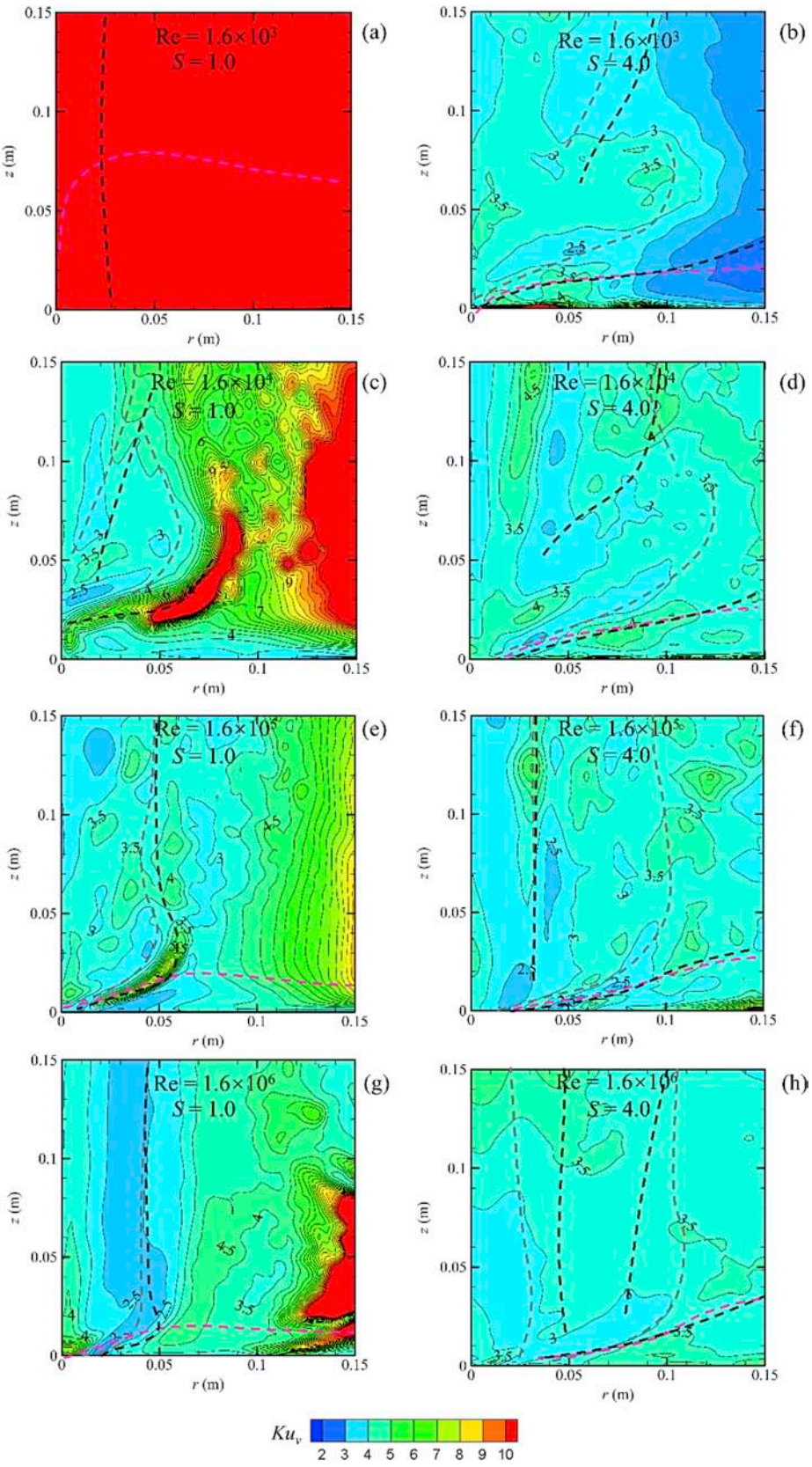

Fig. 21. Distributions of the space averaged kurtosis of the tangential velocity on the vertical slice crossing the center of the tornado (a) R3S1, (b) R3S4, (c) R4S1, (d) R4S4, (e) R5S1, (f) R5S4, (g) R6S1, and (h) R6S4. The pink dashed lines show the depth of the convergence flow determined by the locations with 0.1 U_{max}, and the grey dashed lines indicate the locations the time-space averaged vertical velocity peaks. (For interpretation of the references to color in this figure legend, the reader is referred to the Web version of this article.)

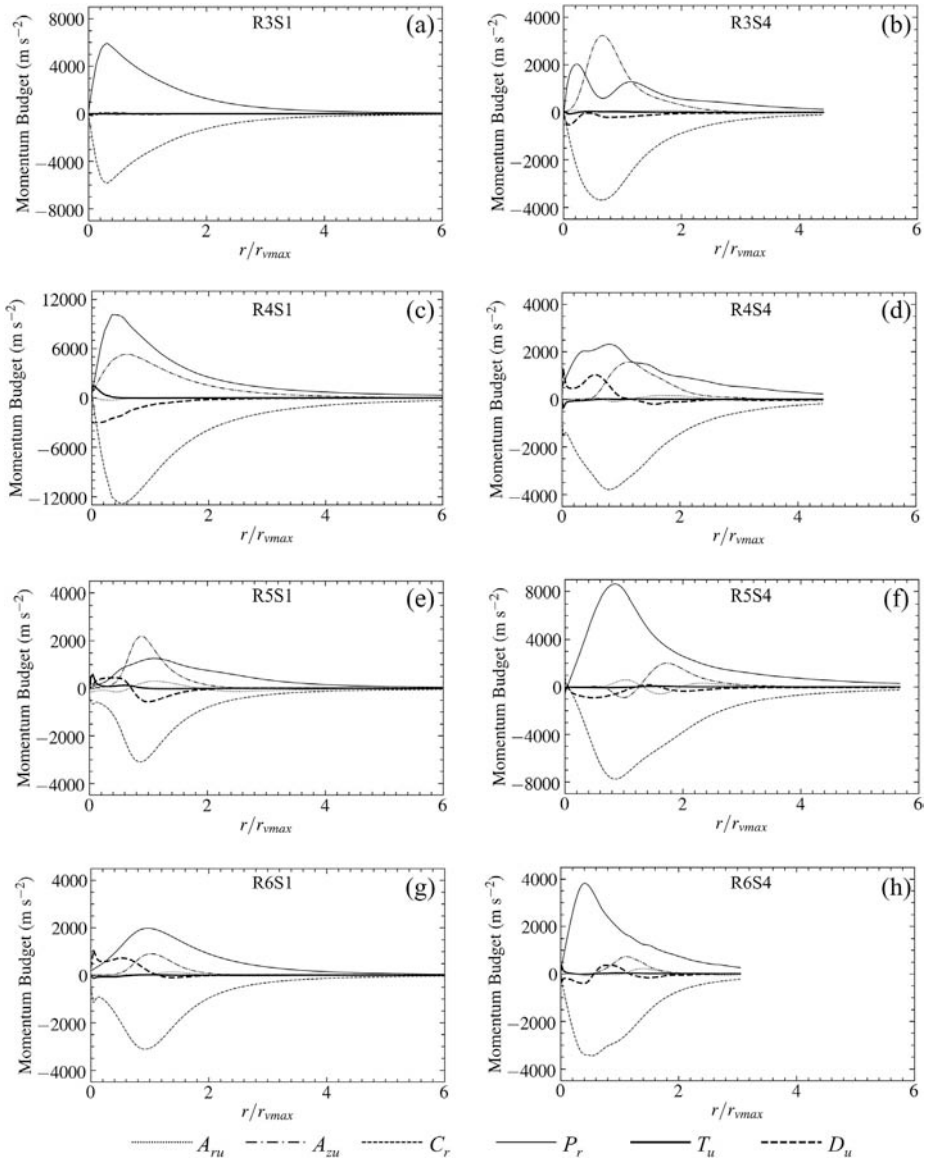

Fig. 22. Radial distributions of momentum budget at the height of h_{vmax} (a) R3S1, (b) R3S4, (c) R4S1, (d) R4S4, (e) R5S1, (f) R5S4, (g) R6S1, and (h) R6S4.

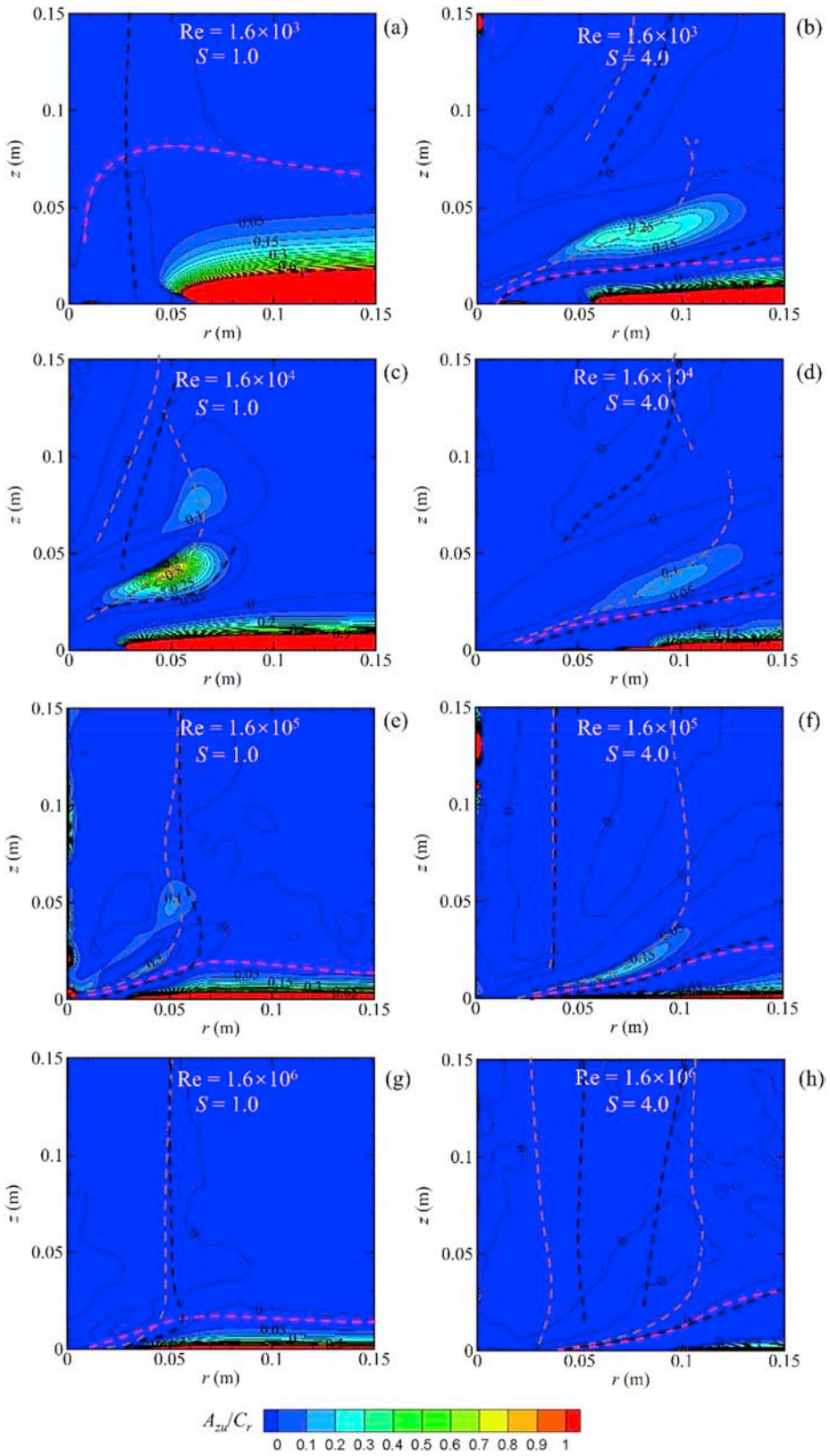

Fig. 23. Distributions of the A_{zu}/C_r on the vertical slice crossing the center of the tornado (a) R3S1, (b) R3S4, (c) R4S1, (d) R4S4, (e) R5S1, (f) R5S4, (g) R6S1, and (h) R6S4.

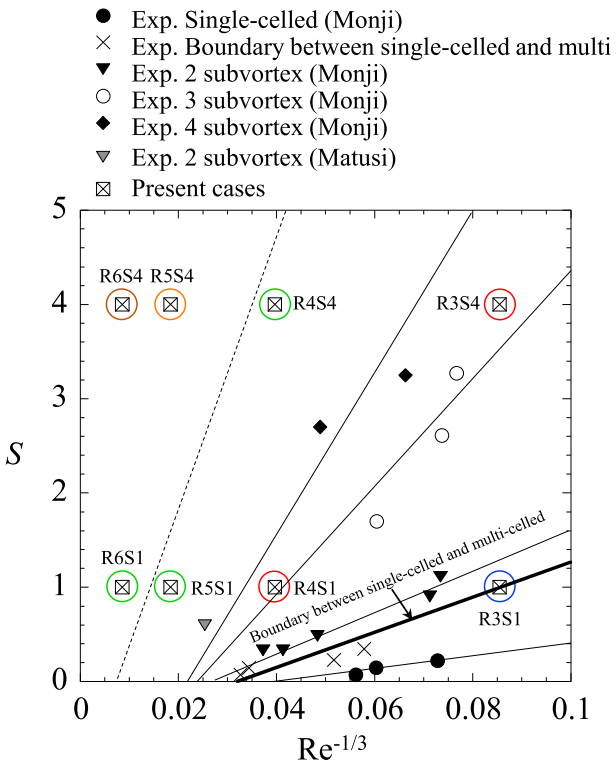

Fig. 24. Distribution of the tornados as a function of S and Re

If k can be set by $1/S$ in an appropriate manner, Eq. (17) should be very useful in the experiments to ascertain S or Re when finding the tornado-like vortices comparable to those in the real situation. Therefore, it should be valuable for the researchers to enrich the diagram in Fig. 25 (b) together.

4. Conclusions

To examine the effects of Reynolds number on the flow fields in tornadoes, eight tornado-like vortices with $S = 1.0$–4.0 and $\mathrm{Re} = 1.6 \times 10^3$–$1.6 \times 10^6$ are numerically modeled by LES. The findings in the present LES are summarized below.

1. For a certain S, the area with obvious turbulence does not significantly vary with Re. The depth of the convergence flow is found to be lower as increasing Re.
2. The penetration of the outer convergence flow to the corner of the tornado tends to be much more difficult, and the location of the peak positive radial velocity is moved outward with the increase in Re.
3. In the outer-core region, the radial fluctuation almost increases linearly with Re. In addition, organized motion of the tornado core is observed no matter how large Re is.
4. If Re is sufficiently high, the major balance between the radial pressure gradient and the centrifugal force even in the region very close to the ground will be reached.
5. h_{vmax}/r_{vmax} shows almost a linear relationship with $\mathrm{Re}^{-1/3}$. Besides, h_{vmax}/r_{vmax} ($\mathrm{Re}^{-1/3}$) decreases in the slope of its curve with increasing in S.

(a) h_{vmax}/r_{vmax}

$\mathrm{Re}^{-1/3}$	S = 1.0	S = 4.0
0.086	7.500	0.500
0.040	1.133	0.240
0.018	0.420	0.125
0.009	0.246	0.067

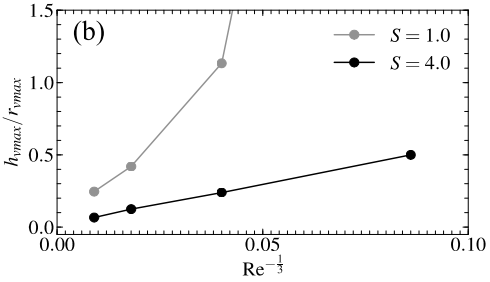

Fig. 25. Variations of h_{vmax}/r_{vmax} as a function of S and Re, (a) table for h_{vmax}/r_{vmax}, and (b) diagram for h_{vmax}/r_{vmax}. The colors in the table indicate the level of h_{vmax}/r_{vmax}. (For interpretation of the references to color in this figure legend, the reader is referred to the Web version of this article.)

non-linear trend in the S(Re) curve, which is worth doing experimental or numerical examinations in the future. In addition, the ground roughness condition [Liu and Ishihara (2016)] as well as the aspect ratio will also have the influence to the flow fields of the tornadoes [Tang et al. (2018)], and further examinations about the effects from these two issues to the S(Re) curve should be carried out in the future.

The macro parameter, h_{vmax}/r_{vmax}, as a function of S and Re is shown in Fig. 25, where Fig. 25a is the matrix of h_{vmax}/r_{vmax} versus S and $\mathrm{Re}^{-1/3}$, and Fig. 25b is the diagram of h_{vmax}/r_{vmax} with x axis being $\mathrm{Re}^{-1/3}$. h_{vmax}/r_{vmax} has been considered as the key parameter to find the counterpart in between the modeled tornadoes with those in full scale, see the study by Refan et al. (2014), and Refan and Hangan (2016). In Fig. 25b, h_{vmax}/r_{vmax} exhibits almost a linear relationship with $\mathrm{Re}^{-1/3}$ except the single-celled tornado. In addition, with increasing S, the slope of the curve h_{vmax}/r_{vmax} versus $\mathrm{Re}^{-1/3}$ decreases. Thus, a formula determining the relationship between h_{vmax}/r_{vmax}, S and Re can be expressed as:

$$h_{vmax}/r_{vmax} = k\ \mathrm{Re}^{-1/3},\ \text{where } k \propto 1/S, \tag{17}$$

Acknowledgement

Z. Liu acknowledges support by the National Natural Science Foundation of China of China (51608220), the Project of Innovation-driven Plan in Huazhong University of Science and Technology (2017KFYXJJ141), and the support from Key Laboratory for Wind and Bridge Engineering of Hunan Province.

References

Ashton, R., Refan, M., Iungo, G., Hangan, H., 2019. Wandering corrections from PIV measurements of tornado-like vortices. J. Wind Eng. Ind. Aerodyn. 189, 163–172.
Baker, G., 1981. Boundary Layer in a Laminar Vortex Flows. PhD Thesis. Purdue University, West Lafayette, USA.
Baker, C., Sterling, M., 2018. A conceptual model for wind and debris impact loading of structures due to tornadoes. J. Wind Eng. Ind. Aerodyn. 175, 283–291.
Cao, S., Wang, M., Cao, J., 2018. Numerical study of wind pressure on low-rise buildings induced by tornado-like flows. J. Wind Eng. Ind. Aerodyn. 183, 214–222.
Cao, J., Ren, S., Cao, S., Ge, Y., 2019. Physical simulations on wind loading characteristics of streamlined bridge decks under tornado-like vortices. J. Wind Eng. Ind. Aerodyn. 189, 56–70.

Case, J., Sarkar, P., Sritharan, S., 2014. Effect of low-rise building geometry on tornado-induced loads. J. Wind Eng. Ind. Aerodyn. 133, 124–134.
Church, C.R., Snow, J.T., Baker, G.L., Agee, E.M., 1979. Characteristics of tornado-like vortices as a function of swirl ratio: a laboratory investigation. J. Atmos. Sci. 36, 1755–1776.
Davies-Jones, R., 1973. The dependence of core radius on swirl ratio in a tornado simulator. J. Atmos. Sci. 30 (7), 1427–1430.
Eguchi, Y., Hattori, Y., Nakao, K., James, D., Zuo, D., 2018. Numerical pressure retrieval from velocity measurement of a turbulent tornado-like vortex. J. Wind Eng. Ind. Aerodyn. 174, 61–68.
Feng, C., Chen, X., 2018. Characterization of translating tornado-induced pressures and responses of a low-rise building frame based on measurement data. Eng. Struct. 174, 495–508.
Ferziger, J., Peric, M., 2002. Computational Method for Fluid Dynamics, third ed. Springer.
Fiedler, B., 2009. Suction vortices and spiral breakdown in numerical simulations of tornado-like vortices. Atmos. Sci. Lett. 10 (2), 109–114.
Gairola, A., Bitsuamlak, G., 2019. Numerical tornado modeling for common interpretation of experimental simulators. J. Wind Eng. Ind. Aerodyn. 186, 32–48.
Hangan, H., Kim, J.-D., 2008. Swirl ratio effects on tornado vortices in relation to the Fujita scale. Wind Struct. 11, 291–302.
Haan, F., Sarkar, P., Gallus, W., 2008. Design, construction and performance of a large tornado simulator for wind engineering applications. Eng. Struct. 30, 1146–1159.
Hu, H., Yang, Z., Sarkar, P., Haan, F., 2011. Characterization of the wind loads and flow fields around a gable-roof building model in tornado-like winds. Exp. Fluid 51, 835–851.
Ishihara, T., Oh, S., Tokuyama, Y., 2011. Numerical study on flow fields of tornado-like vortices using the LES turbulence model. J. Wind Eng. Ind. Aerodyn. 99, 239–248.
Ishihara, T., Liu, Z., 2014. Numerical study on dynamics of a tornado-like vortex with touching down by using the LES turbulence model. Wind Struct. 19, 89–111.
Kashefizadeh, H., Verma, S., Selvam, P., 2019. Computer modelling of close-to-ground tornado wind-fields for different tornado widths. J. Wind Eng. Ind. Aerodyn. 191, 32–40.
Kim, Y., Matsui, M., 2017. Analytical and empirical models of tornado vortices: a comparative study. J. Wind Eng. Ind. Aerodyn. 171, 230–247.
Kuai, L., Haan, F., Gallus, W., Sarkar, P., 2008. CFD simulations of the flow field of alaboratory-simulated tornado for parameter sensitivity studies and comparison with field measurements. Wind Struct. 11, 1–22.
Lewellen, D.C., Lewellen, W.S., Sykes, R.I., 1997. Large-eddy simulation of a tornado's interaction with the surface. J. Atmos. Sci. 54, 581–605.
Lewellen, D.C., Lewellen, W.S., Xia, J., 2000. The influence of a local swirl ratio on tornado intensification near the surface. J. Atmos. Sci. 57, 527–544.
Lewellen, D.C., Lewellen, W.S., 2007. Near-surface intensification of tornado vortices. J. Atmos. Sci. 64, 2176–2194.
Liu, Z., Ishihara, T., 2015a. Numerical study of turbulent flow fields and the similarity of tornado vortices using large-eddy simulations. J. Wind Eng. Ind. Aerodyn. 145, 42–60.
Liu, Z., Ishihara, T., 2015b. A study of tornado induced mean aerodynamic forces on a gable-roofed building by the large eddy simulations. J. Wind Eng. Ind. Aerodyn. 146, 39–50.
Liu, Z., Ishihara, T., 2016. Study of the effects of translation and roughness on tornado-like vortices by large-eddy simulations. J. Wind Eng. Ind. Aerodyn. 151, 1–24.
Liu, Z., Liu, H., Cao, S., 2018. Numerical study of the structure and dynamics of a tornado at the sub-critical vortex breakdown stage. J. Wind Eng. Ind. Aerodyn. 177, 306–326.
Lombardo, F., Roueche, D., Prevatt, D., 2015. Comparison of two methods of near-surface wind speed estimation in the 22 May, 2011 Joplin, Missouri Tornado. J. Wind Eng. Ind. Aerodyn. 138, 87–97.
Maruyama, T., 2011. Simulation of flying debris using a numerically generated tornado-like vortex. J. Wind Eng. Ind. Aerodyn. 99, 249–256.
Matsui, M., Tamura, Y., 2009. Influence of swirl ratio and incident flow conditions on generation of tornado-like vortex. Proc. EACWE 5 (CD-ROM).
Min, C., Choi, H., 1999. Suboptimal feedback control of vortex shedding at low Reynolds numbers. J. Fluid Mech. 401, 123–156.
Mitsuta, Y., Monji, N., 1984. Development of a laboratory simulator for small scale atmospheric vortices. Nat. Disast. Sci. 6, 43–54.
Monji, N., 1985. A laboratory investigation of the structure of multiple vortices. J. Meteorol. Soc. Jpn. 63, 703–712.
Natarajan, D., Hangan, H., 2012. Large eddy simulations of translation and surface roughness effects on tornado-like vortices. J. Wind Eng. Ind. Aerodyn. 104, 577–584.
Nolan, D., Farrell, B., 1999. The structure and dynamics of tornado-like vortices. J. Atmos. Sci. 56, 2908–2936.
Rajasekharan, S., Matsui, M., Tamura, Y., 2012. Dependence of surface pressures on a cubic building in tornado like flow on building location and ground roughness. J. Wind Eng. Ind. Aerodyn. 103, 50–59.
Rajasekharan, G., Matsui, M., Tamura, Y., 2013. Characteristics of internal pressures and net local roof wind forces on a building exposed to a tornado-like vortex. J. Wind Eng. Ind. Aerodyn. 112, 52–57.
Razavi, A., Sarkar, P., 2018. Tornado-induced wind loads on a low-rise building: influence of swirl ratio, translation speed and building parameters. Eng. Struct. 167, 1–12.
Refan, M., Hangan, H., Wurman, J., 2014. Reproducing tornadoes in laboratory using proper scaling. J. Wind Eng. Ind. Aerodyn. 135, 136–148.
Refan, M., Hangan, H., 2016. Characterization of tornado-like flow fields in a new model scale wind testing chamber. J. Wind Eng. Ind. Aerodyn. 151, 107–121.
Refan, M., Hangan, H., 2018. Near surface experimental exploration of tornado vortices. J. Wind Eng. Ind. Aerodyn. 175, 120–135.
Rotunno, R., 1977. Numerical simulation of a laboratory vortex. J. Atmos. Sci. 34, 1942–1956.
Sabareesh, G., Matsui, M., Tamura, Y., 2013. Ground roughness effects on internal pressure characteristics for buildings exposed to tornado-like flow. J. Wind Eng. Ind. Aerodyn. 122, 113–117.
Strasser, M., Yousef, M., Selvam, R., 2016. Defining the vortex loading period and application to assess dynamic amplification of tornado-like wind loading. J. Fluids Struct. 63, 188–209.
Tang, Z., Zuo, D., James, D., Eguchi, Y., Hattori, Y., 2018. Effects of aspect ratio on laboratory simulation of tornado-like vortices. Wind Struct. 27 (2), 111–121.
Tari, P., Gurka, R., Hangan, H., 2010. Experimental investigation of tornado-like vortex dynamics with swirl ratio: the mean and turbulent flow fields. J. Wind Eng. Ind. Aerodyn. 98, 936–944.
Wan, C., Chang, C., 1972. Measurement of the velocity field in a simulated tornado-like vortex using a three-dimensional velocity probe. J. Atmos. Sci. 29, l16–127.
Wang, J., Cao, S., Pang, W., Cao, J., Zhao, L., 2016. Wind-load characteristics of a cooling tower exposed to a translating tornado-like vortex. J. Wind Eng. Ind. Aerodyn. 158, 26–36.
Wang, J., Cao, S., Pang, W., Cao, J., 2017. Experimental study on effects of ground roughness on flow characteristics of tornado-like vortices. Boundary-Layer Meteorol. 162 (2), 319–339.
Ward, N., 1972. The exploration of certain features of tornado dynamics using a laboratory model. J. Atmos. Sci. 29, 1194–1204.
Wilson, T., Rotunno, R., 1986. Numerical simulation of a laminar end-wall vortex and boundary layer. Phys. Fluids 29, 3993–4005.
Yuan, F., Yan, G., Honerkamp, R., Isaac, K., Zhao, M., Mao, X., 2019. Numerical simulation of laboratory tornado simulator that can produce translating tornado-like wind flow. J. Wind Eng. Ind. Aerodyn. 190, 200–217.
Yang, Z., Sarkar, P., Hu, H., 2011. An experimental study of a high-rise building model in tornado-like winds. J. Fluids Struct. 27, 471–486.
Zhang, W., Sarkar, P., 2012. Near-ground tornado-like vortex structure resolved by particle image velocimetry (PIV). Exp. Fluid 52, 479–493.
Zeng, L., Balachandar, S., Fischer, P., 2005. Wall-induced forces on a rigid sphere at finite Reynolds number. J. Fluid Mech. 536, 1–25.
Zhou, H., Dhiradhamvit, K., Attard, T., 2014. Tornado-borne debris impact performance of an innovative storm safe room system protected by a carbon fiber reinforced hybrid polymeric-matrix composite. Eng. Struct. 59, 308–319.